UNIVERSITY OF ROCHESTER
LABORATORY FOR LASER ENERGETICS

Volume 161
October–December 2019
DOE/NA/3856-1550

LLE Review

Quarterly Report

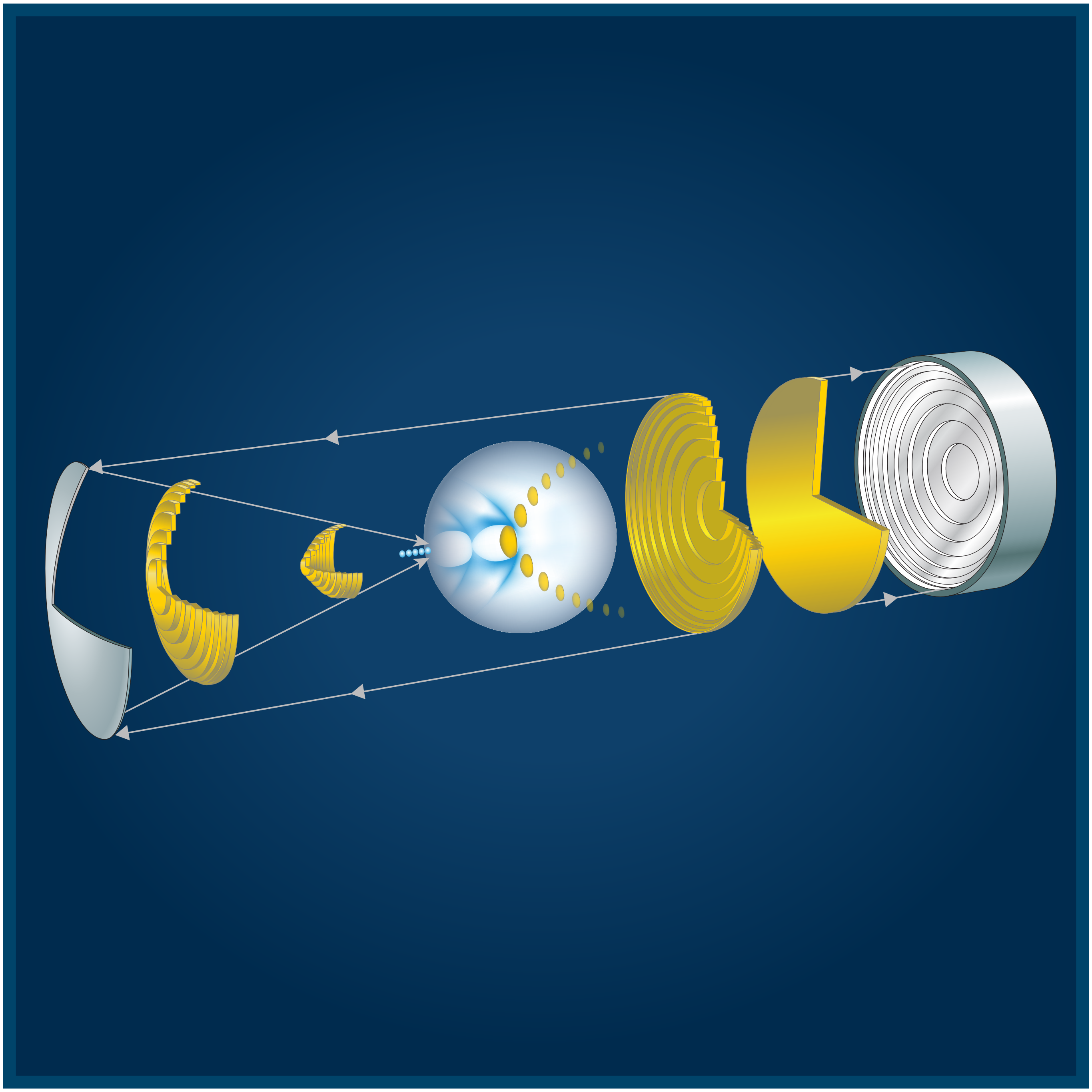

About the Cover:

The cover depicts a new technique for spatiotemporal pulse shaping that enables dephasingless laser wakefield acceleration (see p. 10). The laser pulse first hits a cylindrically symmetric echelon (far right, also shown in the figure to the right) that is used to adjust the relative temporal delay of each radial point of the near field. After reflecting off of the echelon, the pulse hits an axiparabola, an optic that creates an extended focal region where the pulse can sustain high intensity (far left). Overall, this novel technique delivers an ultrashort pulse to each axial location in the long focal region without introducing chromatic aberration.

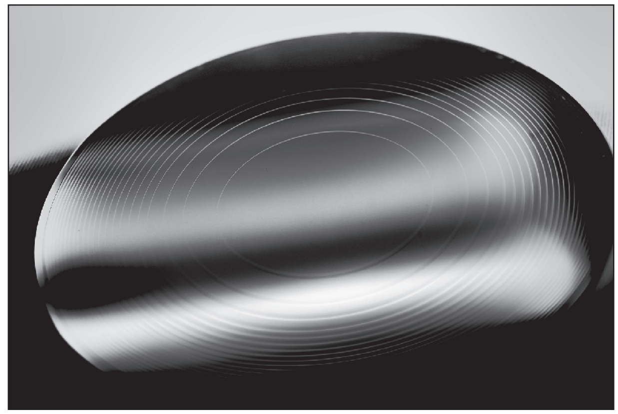

The work described in this volume includes current research at the Laboratory for Laser Energetics, which is supported by New York State Energy Research and Development Authority, the University of Rochester, the U.S. Department of Energy Office of Inertial Confinement Fusion under Cooperative Agreement No. DE-NA0003856, and other agencies.

Printed in the United States of America
Available from
National Technical Information Services
U.S. Department of Commerce
5285 Port Royal Road
Springfield, VA 22161
www.ntis.gov

For questions or comments, contact Katelynn Bauer, Editor, Laboratory for Laser Energetics, 250 East River Road, Rochester, NY 14623-1299, (585) 276-5618.

www.lle.rochester.edu

UNIVERSITY OF ROCHESTER
LABORATORY FOR LASER ENERGETICS

Volume 161
October–December 2019
DOE/NA/3856-1550

LLE Review

Quarterly Report

Contents

In Brief

This volume of LLE Review 161, covering the period October–December 2019, is sectioned among research areas at LLE and external users of the Omega Laser Facility. Articles appearing in this volume are the principal summarized results of long-form research articles. Readers seeking a more-detailed account of research activities are invited to seek out the primary materials appearing in print, detailed in the publications and presentations section at the end of this volume.

Highlights of research presented in this volume include the following:

- K. M. Woo *et al.* demonstrate that it is possible to infer the thermal ion temperature from nuclear measurements (p. 1). The inferred DD minimum ion temperatures demonstrate a strong correlation with the experimental yields in the OMEGA implosion database.

- H. G. Rinderknecht *et al.* describe the asymmetry limits of inertial confinement fusion implosions at the National Ignition Facility (NIF) (p. 3). Analysis of hot-spot plasma flows and areal densities point to an unexpected low-mode asymmetry. Investigation into causes of this asymmetry is ongoing.

- X. Bian *et al.* perform simulations of the effects of perturbation Reynolds number and Atwood number on the late-time growth of the Rayleigh–Taylor instability (p. 7). The analysis shows a strong correlation between vorticity and bubble velocity.

- J. P. Palastro *et al.* design a dephasingless laser wakefield accelerator (p. 10). A spatiotemporal technique is described and shown to deliver an ultrashort pulse without chromatic aberrations.

- R. K. Follett *et al.* present 3-D calculations of multibeam absolute stimulated Raman scattering thresholds (p. 13). The multibeam coupling is shown to be weaker for stimulated Raman scattering than two-plasmon decay, consistent with OMEGA and NIF experiments.

- D. Haberberger *et al.* discuss a novel high-temperature Raman amplifier where laser–plasma instabilities are mitigated (p. 16).

- A. Kar *et al.* describe a microphysics model for hydrodynamic simulations (p. 19). Implementation of this model predicts higher values of electron density and pressure than the previously used *ad hoc* model.

- S. X. Hu *et al.* apply a thermal density function theory to investigate the radiation spectra of superdense plasma mixtures (p. 23). Calculations reveal interspecies and dipole-forbidden transitions that were not previously considered.

- M. J. Rosenberg *et al.* discuss stimulated Raman scattering mechanisms on the NIF (p. 25). Tangential sidescatter and near-backscatter were observed at lower densities.

- L. S. Leal *et al.* discuss a series of *HYDRA* simulations to model magnetic confinement of a laser-generated plasma (p. 28). It is shown that applying strong external fields to laser-generated plasmas leads to complex plasma structures.

- J. L. Peebles *et al.* demonstrate the diagnostic technique of axial proton probing of a laser-driven coil (p. 31).

- S. Zhang, H. D. Whitley, and T. Ogitsu calculate the equation of state and shock Hugoniot of various boron phases (p. 37). Results indicate inconsistency between Hugoniots of the equilibrium phases and those measured by shock experiments.

- O. M. Mannion *et al.* describe a suite of neutron time-of-flight detectors (p. 40). By combining neutron velocity measurements made by each detector, the neutron-averaged hot-spot velocity has been measured for the first time on OMEGA.

- T. Filkins and J. Katz present a design for a free-space, image-relay optical time domain reflectometer (p. 43). The uncertainty of the fiber-optic time delay is determined to be approximately 2 ps.

- J. Puth *et al.* summarize operations of the Omega Laser Facility during the first quarter of FY20 (p. 45).

Katelynn Bauer
Editor

Inferring Thermal Ion Temperature and Residual Kinetic Energy from Nuclear Measurements in Inertial Confinement Fusion Implosions

K. M. Woo,[1,2] R. Betti,[1,2,3] O. M. Mannion,[1,2] C. J. Forrest,[1] J. P. Knauer,[1] V. N. Goncharov,[1] P. B. Radha,[1] D. Patel,[1,3] V. Gopalaswamy,[1,3] and V. Yu. Glebov[1]

[1]Laboratory for Laser Energetics, University of Rochester
[2]Department of Physics & Astronomy, University of Rochester
[3]Department of Mechanical Engineering, University of Rochester

In inertial confinement fusion (ICF) implosion experiments, the presence of residual anisotropic fluid motion within the stagnating hot spot leads to significant variations in ion-temperature measurements using neutron time-of-flight detectors along different lines of sight (LOS's). The minimum of measured ion temperatures is typically used as representative of the thermal temperature. In the presence of isotropic flows, however, even the minimum DT neutron-inferred ion temperature can be well above the plasma thermal temperature. Consequently, apparent ion temperatures, which are inferred from the width of neutron energy spectra,[1] are larger than the real thermal ion temperature. This leads to underestimating the inferred hot-spot pressures used as a metric to measure ICF implosion performance.

The influence of 3-D flow effects on apparent ion temperatures is governed by the properties of velocity variance, contributed by both isotropic and anisotropic flows. To describe this phenomenon, the method of velocity variance decomposition[2] is applied. The fluid velocity vector and the LOS unit vector are substituted into the velocity variance, followed by an expansion into six components. The resulting apparent ion temperatures can be rewritten as

$$T_{\mathrm{i}}^{\mathrm{inferred}} = T_{\mathrm{i}}^{\mathrm{thermal}} + M_{\mathrm{DT}} \sum_{i,j=1}^{3} g_i g_j \sigma_{ij}. \tag{1}$$

Here M_{DT} is the DT total reactant mass. The indices 1, 2, and 3 correspond to Cartesian coordinates x, y, and z, respectively; $\hat{e}_i$ is an orthonormal unit vector. Three geometrical factors—$g_1 = \sin\theta\cos\phi$, $g_2 = \sin\theta\sin\phi$, and $g_3 = \cos\theta$—specify the polar θ and azimuthal ϕ angles for a given LOS. The six components of the fluid velocity variance $\sigma_{ij} = \langle \Delta v_i \Delta v_j \rangle$ measure the flow structure within the hot spot, where $\Delta v_i = v_i - \langle v_i \rangle$ is the velocity fluctuation along the ith direction with respect to the mean velocity $\langle v_i \rangle$. The covariances σ_{12}, σ_{23}, and σ_{31} measure the degree of azimuthal asymmetry. The directional variances σ_{11}, σ_{22}, and σ_{33} are proportional to the nontranslational component of the hot-spot fluid kinetic energy, i.e., $\sigma_{ii} = \langle \Delta v_i^2 \rangle$.

Equation (1) describes the nonrelativistic, 3-D hot-spot flow asymmetry on neutron-inferred ion-temperature measurements. The variation in ion-temperature measurements along different LOS's is uniquely governed by the content of the fluid (residual) kinetic energy (RKE) and the properties of the hot-spot flow structure. For turbulent flows, the vanishing covariances lead to apparent ion temperatures inflated uniformly in 4π caused by the isotropic hot-spot fluid kinetic energies from the radial component of the flows. The 4π minimum of the velocity variance is the fundamental isotropic source contributed by fluid properties that causes the minimum apparent ion temperatures above the real thermal ion temperatures. Equation (1) reveals that the solution for the real thermal ion temperature can be derived by performing DD and DT ion-temperature measurements at a given set of LOS's to form an invertible matrix.

Figure 1(a) shows the strong correlation between the D–T experimental yields and the derived DD minimum ion temperatures in the OMEGA implosion database. The strong dependence on the DD minimum ion temperatures leads to yields that scale with ion temperatures $\sim T^{3.96}$ close to the power of 4. The minimum of DD ion temperature is closer to the real thermal ion temperature because the DD total fusion reactant mass $M_{DD} \simeq 0.8 M_{DT}$ is smaller than that of DT's, resulting in a smaller contribution of isotropic flows in T_{min}^{DD}. Consider a simultaneous ion-temperature measurement for DD and DT along the same single LOS: $T_{LOS}^{DT} = T_{min}^{DT} + M_{DT}\sigma_{aniso}^{DT}$ and $T_{LOS}^{DD} = T_{min}^{DD} + M_{DD}\sigma_{aniso}^{DD}$; the minimum DD ion temperature can be derived by removing the common part of the anisotropic velocity variance σ_{aniso}.

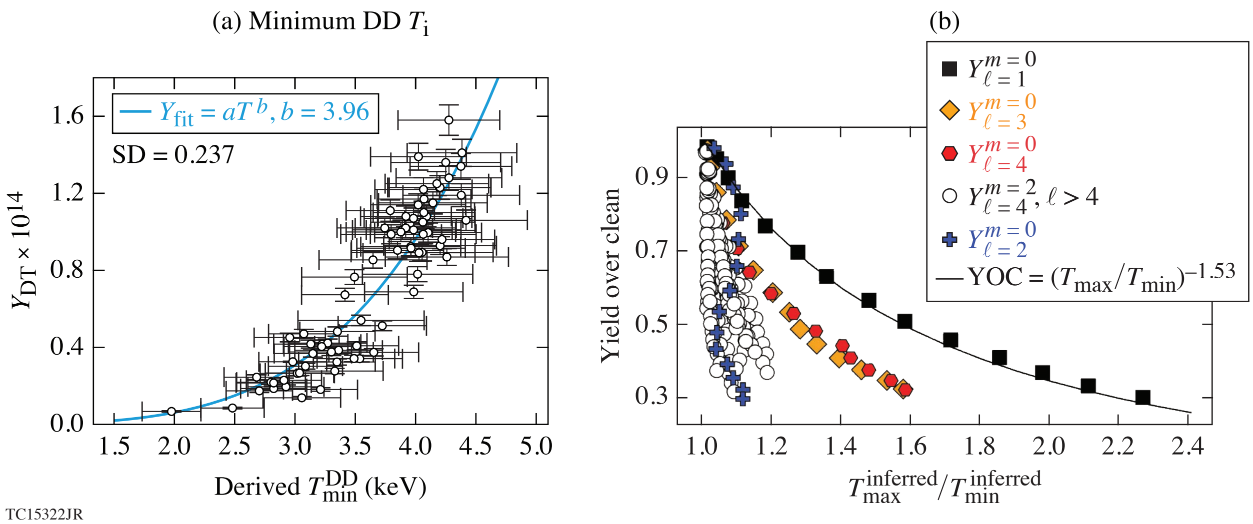

Figure 1

(a) Comparison between the experimental D–T yields with the derived DD minimum ion temperatures. (b) Comparison between the simulated YOC with the ratio of the inferred maximum to the inferred minimum ion temperatures for single modes $\ell = 1$ to 10.

Figure 1(b) compares the yield-over-clean (YOC) with the ratio of the inferred maximum to the inferred minimum ion temperatures for single modes $\ell = 1$ to 10. The YOC is shown to be less sensitive with increasing Legendre mode numbers. A good agreement is observed between the yield degradation and the analytic curve: YOC $\simeq \left(T_{max}/T_{min}\right)^{-1.53}$, derived using Eq. (1). This result explains the effect of mode-1 ion-temperature asymmetries in terms of residual kinetic energies: $\left(T_{max}/T_{min}\right)_{\ell=1} = 1 + 4\text{RKE}/(1\text{–RKE})$, where RKE is given by the ratio of the difference of fluid kinetic energies at stagnations between 3-D and 1-D to the maximum 1-D in-flight fluid kinetic energy.

This material is based upon work supported by the Department of Energy National Nuclear Security Administration under Award Number DE-NA0003856, the University of Rochester, and the New York State Energy Research and Development Authority.

1. H. Brysk, Plasma Phys. **15**, 611 (1973).

2. K. M. Woo *et al.*, Phys. Plasmas **25**, 102710 (2018).

Azimuthal Drive Asymmetry in Inertial Confinement Fusion Implosions at the National Ignition Facility

H. G. Rinderknecht,[1] D. T. Casey,[2] R. Hatarik,[2] R. M. Bionta,[2] B. J. MacGowan,[2] P. Patel,[2] O. L. Landen,[2] E. P. Hartouni,[2] and O. A. Hurricane[2]

[1]Laboratory for Laser Energetics, University of Rochester
[2]Lawrence Livermore National Laboratory

The large radial convergence required for hot-spot ignition places demanding requirements on the symmetry of implosions. Asymmetric convergence of an inertial confinement fusion (ICF) implosion is predicted to generate unstagnated flows in the converged fuel and hot spot, which limits the maximum hot-spot pressure and reduces confinement time.[1] An offset drive illuminating one side of a capsule more brightly than the opposite can produce a net velocity in the fusing hot spot and significant asymmetry in fuel assembly.[2] Hot-spot flows have been measured using time-resolved x-ray pinhole cameras,[3] but the accuracy of this technique is limited by the small number of diagnostic views. Asymmetry in the assembled fuel has been suggested by trends in hot-spot areal density, ion temperature, and pressure,[4] and from significant variations of scattered neutron flux with line of sight observed on some implosions.[5] In this work, nuclear diagnostics were found to present a strong signature of a systematic mode-1 drive asymmetry in the cryogenic implosion campaigns performed at the National Ignition Facility (NIF) from 2016–2018. The observed asymmetry limits the performance of the present ICF implosions and must be corrected if ignition is to be achieved.

Flows in the hot-spot plasma are diagnosed by measuring the Doppler shift of the fusion neutrons. A neutron-averaged flow velocity projected along each of four neutron time-of-flight detector lines of sight is obtained by measuring the shift in mean neutron energy relative to the expected value.[6] The mean hot-spot velocity magnitude and direction are obtained from these measurements, as shown in Fig. 1(a) for 44 shots performed during 2016–2018. For implosions in which significant velocity was inferred ($v > 30$ km/s, a typical value for the measurement uncertainty), the hot spots are observed to flow toward one hemisphere (approximately $-20° < \phi < 160°$). This data set includes experiments that use a variety of laser pulse shapes and ablators, including shots from the high-density carbon (HDC), "Bigfoot" (high-adiabat HDC), and CH campaigns.[7] It is worth noting the magnitude of the velocities observed: many of the implosions presented velocities in excess of 20% of the implosion velocity (typically 350 to 420 km/s), representing significant perturbations to the implosions' uniformity.

The areal density (ρR) of the assembled fuel is diagnosed by a suite of neutron activation diagnostics on over 20 lines of sight. Activation of Zr-90 atoms records the fluence of unscattered neutrons above 12 MeV, which is inversely proportional to ρR after correcting for the effects of the Doppler shift on the measurement.[8] If scattered neutrons are assumed to be lost from detection, the variation in areal density ($\Delta\rho R$) can be calculated from the variation in activation A relative to the mean value $\langle A \rangle$ as

$$\Delta\rho R \approx -\frac{M_{\mathrm{DT}}}{\sigma_{\mathrm{DT}}}\ln\left(\frac{A}{\langle A\rangle}\right) \sim -\ln\left(\frac{A}{\langle A\rangle}\right) 4.64\ \mathrm{g/cm}^2. \tag{1}$$

Performing the activation analysis for the 2016–2018 NIF cryogenic experiments produces a similar pattern to that observed in the velocity data. The inferred areal-density asymmetry [from Eq. (1)] normalized to the average areal density is plotted in Fig. 1(b) compared with the measured hot-spot velocity. The magnitudes of the two signatures are observed to scale linearly across the entire data set: a best-fit slope of 39% ρR mode-1 asymmetry per 100-km/s hot-spot velocity matches the data with a reduced

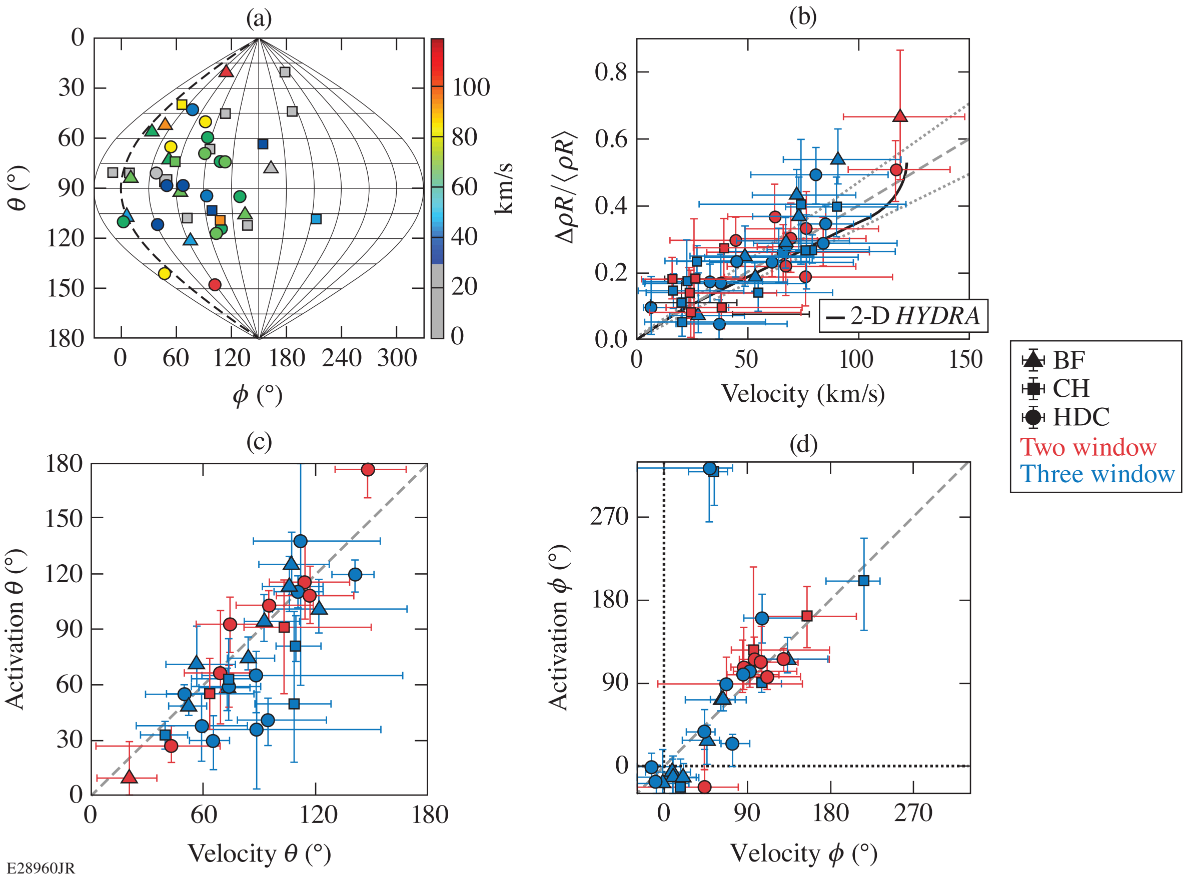

Figure 1
(a) The measured hot-spot velocity for 43 implosions performed on the NIF from 2016–2018. Most shots in the data set (32) present significant hot-spot velocity (v > 30 km/s) clustering in one hemisphere. (b) Mode-1 variation in areal density ($\Delta\rho R/\rho R$) compared with measured hot-spot velocity (km/s). Areal-density variation scales linearly with velocity, in agreement with a 2-D *HYDRA* model including mode-1 drive asymmetry (black line). [(c),(d)] The inferred (θ, ϕ) direction of maximum activation (minimum ρR) compared with hot-spot velocity. Implosions with two-window hohlraums (red symbols) cluster toward ϕ = 94°±35°, whereas those with three-window hohlraums (blue symbols) cluster toward ϕ = 58°±53°.

χ^2 metric of 0.3. Moreover, the direction of high activation (low areal density) was found to match the direction of the hot-spot velocity, as shown in Figs. 1(c) and 1(d). The hypothesis that the (θ, ϕ) directions of the hot-spot velocity and activation mode-1 are the same is supported with reduced χ^2 values of 0.7 and 0.6, respectively. (These low values of the reduced χ^2 metric suggest that the measurement uncertainties are likely overestimated.) The comparison of the azimuthal angle in Fig. 1(d) clearly shows the clustering of data points into the range $-20° \lesssim \phi \lesssim 160°$. The implosions used hohlraums with diagnostic windows (regions of the hohlraum wall with thinner gold layers) toward ϕ = 78° and 99° ["two-window" (red)] and with an additional window toward ϕ = 314° ["three-window" (blue)], which cluster toward different directions. The two-window hohlraums are observed to produce hot-spot velocities on average in the direction ϕ = 94°±35°, whereas three-window hohlraums produce velocities toward ϕ = 58°±53°. These values are consistent with the average of the window directions in each design, suggesting the windows contribute to the observed trend.

These observations together strongly indicate the presence of an unexpected systematic implosion asymmetry in NIF cryogenic implosions over the past three years. Spears *et al.*[2] performed 2-D simulations of indirectly driven implosions with an imposed mode-1 asymmetry in the radiation intensity that produced a trend consistent with our observations. While this work was motivated by the possibility of pole-to-pole asymmetry, the result does not consider hohlraum geometry and is generally applicable to radiation asymmetry in arbitrary directions. The drive asymmetry accelerated the capsule away from the direction with higher radiation flux, producing a neutron-weighted hot-spot velocity in that direction that scaled with the flux asymmetry and covered the range we observed (≤120 km/s). Areal density also increased in the direction of peak intensity and decreased in the opposite direction. A prediction of the scaling between neutron-inferred hot-spot velocity and areal-density asymmetry magnitude [black line in Fig. 1(b)] agrees with the data.

The hohlraum windows can plausibly create such a mode-1 radiation asymmetry. Figure 2 shows a calculation of the reduction in radiation flux onto a capsule inside a three-window hohlraum, assuming complete radiation loss at the windows, performed using the view factor code VisRAD.[9] Up to 6.2% radiation deficit toward the windows is predicted in this limiting case: significantly larger than the asymmetry needed to explain the most extreme velocities. In experiments, thinner gold layers and gaps approaching half the window area will reduce local radiation power by some fraction of this amount, inducing velocity and higher activation in the average direction of the windows. This hypothesis matches the observed data trends with hohlraum window design. Together, these observations provide strong evidence that a systematic, azimuthally directed mode-1 drive asymmetry of up to ±2% in radiation intensity is present in this series of implosions. Detailed models are in development to more quantitatively assess window radiation losses, including the effects of window architecture and ablation dynamics.[10,11]

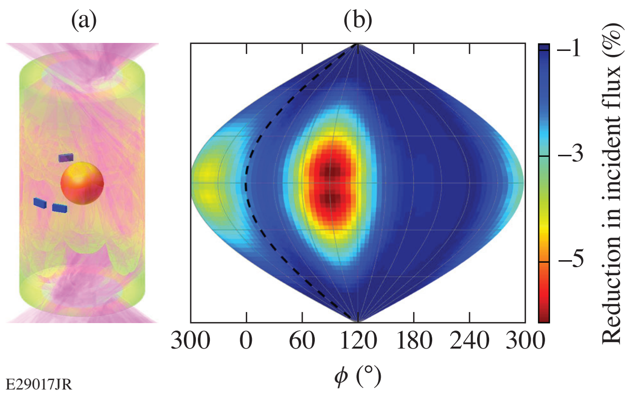

Figure 2
(a) Model of the capsule in a laser-irradiated hohlraum from view angle (65°, 120°). Size and position of diagnostic windows are shown in blue. (b) Calculated reduction of radiation flux on the capsule in a three-window hohlraum, assuming complete radiation loss through windows.

Such an asymmetry represents a dominant degradation mechanism for the implosions: a 3-D model predicts that the implosion asymmetry reduced the yield by 5× for a representative shot in this data set.[1] Investigation of asymmetry sources, including hohlraum windows, laser delivery, capsule and ice-thickness variations, and target alignment is ongoing to improve implosion symmetry control and performance.

This material is based upon work supported by the Department of Energy National Nuclear Security Administration under Award Number DE-NA0003856, the University of Rochester, and the New York State Energy Research and Development Authority.

1. P. T. Springer *et al*., Nucl. Fusion **59**, 032009 (2019).
2. B. K. Spears *et al*., Phys. Plasmas **21**, 042702 (2014).
3. J. J. Ruby *et al*., Phys. Plasmas **23**, 072701 (2016).
4. O. A. Hurricane *et al*., Nat. Phys. **12**, 800 (2016).
5. C. B. Yeamans and N. Gharibyan, Rev. Sci. Instrum. **87**, 11D702 (2016).

6. R. Hatarik *et al*., Rev. Sci. Instrum. **89**, 10I138 (2018).

7. L. Berzak Hopkins *et al*., Plasma Phys. Control. Fusion **61**, 014023 (2018); D. T. Casey *et al*., Phys. Plasmas **25**, 056308 (2018); O. A. Hurricane *et al*., Phys. Plasmas **26**, 052704 (2019).

8. H. G. Rinderknecht *et al*., Rev. Sci. Instrum. **89**, 10I125 (2018).

9. J. J. MacFarlane, J. Quant. Spectrosc. Radiat. Transf. **81**, 287 (2003).

10. B. J. McGowan *et al*., "Trending Low Mode Asymmetries in NIF Capsule Drive Using a Simple Viewfactor Metric," submitted to High Energy Density Physics.

11. J. Milovich *et al*., Bull. Am. Phys. Soc. **64**, JO7.00005 (2019).

Revisiting the Late-Time Growth of Single-Mode Rayleigh–Taylor Instability and the Role of Vorticity

X. Bian,[1] H. Aluie,[1,2] D. Zhao,[1,2] H. Zhang,[1,2] and D. Livescu[3]

[1]Department of Mechanical Engineering, University of Rochester
[2]Laboratory for Laser Energetics, University of Rochester
[3]Los Alamos National Laboratory

The Rayleigh–Taylor instability (RTI) appears at a perturbed interface when a light fluid (ρ_l) is accelerated against a heavy fluid (ρ_h). It can significantly degrade a target's performance in inertial confinement fusion. In Ref. 1 Layzer predicted the nonlinear stage development on assuming a potential flow with Atwood number $A \equiv (\rho_h - \rho_l) / (\rho_h + \rho_l) = 1$. Later, in Ref. 2, Goncharov generalized Layzer's theory to arbitrary Atwood numbers. The model predicts a terminal bubble velocity of $U_\mathrm{b} = 2Ag / [(1+A)Ck]$, where $C = 3$ in 2-D and $C = 1$ in 3-D; k is the perturbation wave number.

Recent studies have shown the limitation of potential flow models in both ablative[3,4] and classical RTI.[5–7] In this study, we perform high-resolution, fully compressible simulations with the highest resolution (1024×8192 in 2-D and $256 \times 256 \times 2048$ in 3-D). The late-time behavior of bubbles and spikes is studied systemically at both low and high Atwood numbers at different perturbation Reynolds numbers:

$$\mathrm{Re_p} \equiv \lambda \sqrt{\frac{A}{1+A} g\lambda} \bigg/ (\mu / \rho_I),$$

where λ is the perturbation wavelength, g is gravity, and ρ_I is the interfacial density. A comparison between 2-D and 3-D RTI is also conducted.

As shown in Fig. 1(a), the analysis of $\mathrm{Re_p}$ suggests that (1) at sufficiently large $\mathrm{Re_p}$, the enhancement in bubble velocity beyond the "terminal" value is sustained and does not decrease at later times, as had been previously observed in lower-resolution simulations,[6] and (2) even at lower $\mathrm{Re_p}$, when the re-acceleration fails or is not achieved altogether, the bubble velocity does not maintain a constant value but decays instead at late times.

Figure 1(b) shows that increasing A makes it more difficult for bubble speed to increase and persist above the "terminal velocity" value of potential flow theory. This is consistent with the findings of Ramaprabhu *et al.*[6] However, Ramaprabhu *et al.*[6] showed an eventual deceleration back to the terminal velocity after a transient re-acceleration stage for all Atwood numbers. In contrast, our results indicate that the bubble speed enhancement above the terminal value can be sustained regardless of A if the $\mathrm{Re_p}$ is sufficiently large. The differing results are most probably caused by the difference in resolution and our code guaranteeing momentum conservation. The results reported here maintain symmetry, which is necessary for momentum conservation, and are at a significantly higher resolution than what was possible several years ago when the study by Ramaprabhu *et al.*[6] was conducted. Compared to the simulations in Ref. 6, our simulations show a clear and sustained bubble-speed enhancement at $A = 0.04$ and 0.25. At $A > 0.25$, the bubble velocity exhibits intermittent oscillations above the terminal value with an intensity that increases with increasing $\mathrm{Re_p}$, suggesting that a clear sustained bubble-speed enhancement is possible if $\mathrm{Re_p}$ is sufficiently large.

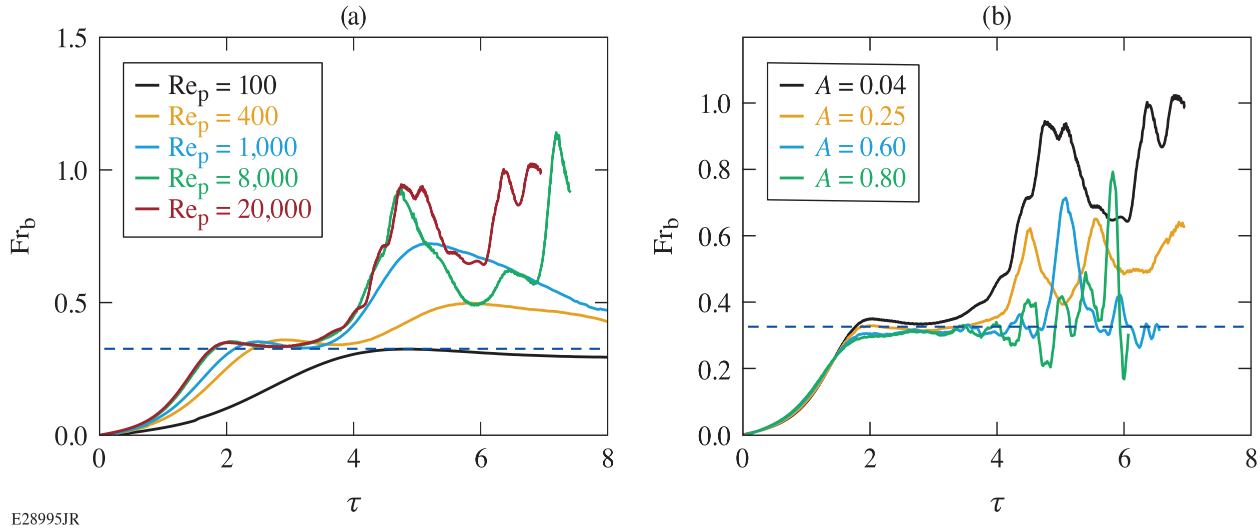

Figure 1
(a) The effects of Re_p on the bubble velocity in 2-D RTI at $A = 0.04$; (b) effects of A on the bubble velocity in 2-D RTI at $Re_p = 20{,}000$. The dashed lines in (a) and (b) show the potential model prediction. Fr_b is the nondimensional bubble velocity; τ is the nondimensional time.

Three-dimensional density visualizations are shown in Fig. 2. The effects of A and Re_p on RTI are qualitatively similar in 2-D and 3-D; however, 3-D bubbles are easier to re-accelerate, having a lower Re_p threshold for any A.

The strong correlation between vorticity and bubble velocity suggests that re-acceleration and deceleration of the bubble front is determined by vorticity accumulation inside the bubble, consistent with the previous findings.[3,7] Here, we quantitatively show that the vortices that propel the bubble front are not generated inside the bubble but are instead generated far below the bubble tip. The vortices then propagate toward the bubble tip. Note that the vortices need to move faster than the bubble tip, which implies that the induced vortical velocity should enhance the advection velocity.

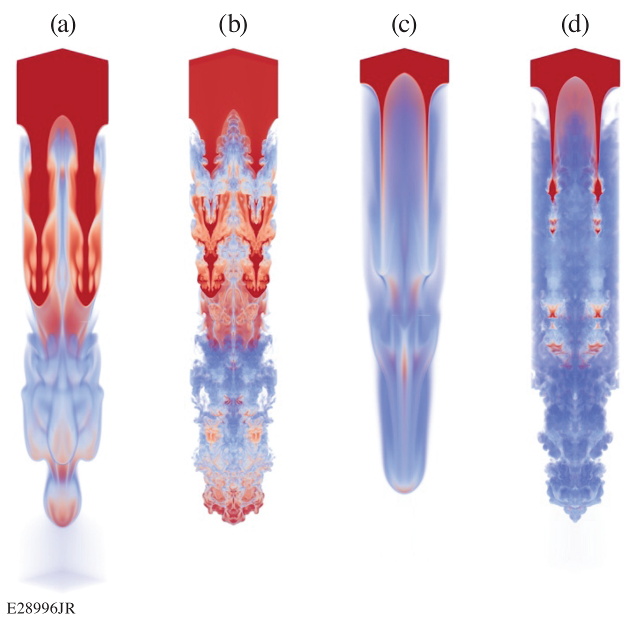

Figure 2
Three-dimensional density visualization at $\tau = 5$. [(a),(b)] Results at $A = 0.04$ for $Re_p = 1000$ and 8000, respectively; [(c),(d)] results at $A = 0.8$ for $Re_p = 1000$ and 8000, respectively.

This research was funded by the LANL LDRD program through project number 20150568ER and DOE FES grant number DE-SC0014318. D. Zhao and H. Aluie were also supported by DOE NNSA award DE-NA0003856. H. Aluie was also supported by NASA grant 80NSSC18K0772 and DOE grant DE-SC0019329. Computing time was provided by the National Energy Research Scientific Computing Center (NERSC) under Contract No. DE-AC02-05CH11231.

1. D. Layzer, Astrophys. J. **122**, 1 (1955).
2. V. N. Goncharov, Phys. Rev. Lett. **88**, 134502 (2002).
3. R. Betti and J. Sanz, Phys. Rev. Lett. **97**, 205002 (2006).
4. R. Yan *et al*., Phys. Plasmas **23**, 022701 (2016).
5. P. Ramaprabhu *et al*., Phys. Rev. E **74**, 066308 (2006).
6. P. Ramaprabhu *et al*., Phys. Fluids **24**, 074107 (2012).
7. T. Wei and D. Livescu, Phys. Rev. E **86**, 046405 (2012).

Dephasingless Laser Wakefield Acceleration

J. P. Palastro,[1] J. L. Shaw,[1] P. Franke,[1,2] D. Ramsey,[1,2] T. T. Simpson,[1,2] and D. H. Froula[1,2]

[1]Laboratory for Laser Energetics, University of Rochester
[2]Department of Physics & Astronomy, University of Rochester

Forty years ago, Tajima and Dawson recognized that the axial electric fields of ponderomotively driven plasma waves far surpass those of conventional radio-frequency accelerators,[1] launching the field of "advanced accelerators"—disruptive concepts that promise smaller-scale, cheaper accelerators for high-energy-physics experiments and advanced light sources. Since their seminal paper, a number of theoretical breakthroughs and experimental demonstrations of laser wakefield acceleration (LWFA) have made rapid progress toward that goal. In spite of the impressive progress, traditional LWFA faces a key design limitation of electrons outrunning the accelerating phase of the wakefield or dephasing.

In traditional LWFA, a near-collimated laser pulse, either through channel or self-guiding, produces a ponderomotive force that travels subluminally at the group velocity ($v_g < c$). The phase velocity of the resulting wakefield equals the velocity of the ponderomotive force. As a result, high-energy electrons traveling at near the vacuum speed of light ($v_e \simeq c$) escape the accelerating phase of wakefield after a dephasing length $L_d \propto n_0^{-3/2}$, where n_0 is the plasma density. Because the maximum accelerating field scales as $E_{max} \propto n_0^{1/2}$, a lower plasma density will increase the maximum energy gain of electrons, $\Delta\gamma \propto n_0^{-1}$, but will greatly increase the length of the accelerator.[2] As an example, a single-stage 1-TeV accelerator would require at least 200 m of uniform, low-density plasma, the creation of which would represent a technical feat unto itself. Instead, the current paradigm within the LWFA community envisions a TeV LWFA composed of multiple ~10-GeV stages. This approach, however, comes with its own set of challenges, such as precisely timing the injection of the electron beam and laser pulses into each of the stages.

We envision something different: a dephasingless laser wakefield accelerator (DLWFA) enabled by a novel optical technique for spatiotemporal pulse shaping that provides control over the phase velocity of the wakefield while preserving the ultrashort duration of the ponderomotive force. In the nonlinear regime ($a_0 > 1$, where $a_0 = eA/m_e c$ is the normalized vector potential of the laser), a DLWFA can achieve TeV energy gains in only 4.5 m—40× shorter than traditional LWFA. Simulations in the linear regime ($a_0 < 1$) demonstrate a 1.3-GeV energy gain in *~3.5× less distance* than a traditional LWFA (8 cm versus 28 cm). The optical technique combines the recently described axiparabola[3] with a novel echelon optic. The axiparabola creates an extended focal region, while the echelon adjusts the temporal delay to provide the desired ponderomotive velocity. This concept improves upon the chromatic flying focus[4] by providing the original features of a small focal spot that can propagate at any velocity over any distance while using an achromatic focusing system to maintain a transform-limited pulse duration ideal for LWFA. Further, by adjusting the profile of the echelon, the ponderomotive force can be made to follow a dynamic trajectory, with either accelerations or decelerations to control trapping and reduce dark current.

Figure 1(a) highlights the advantage of the DLWFA in the linear regime by comparing the energy gains as a function of accelerator length for a DLWFA, a traditional LWFA, and a conventional radio-frequency accelerator. The advantage of the DLWFA increases with the energy gain or accelerator length, i.e., the DLWFA achieves the same energy as a traditional LWFA with an increasingly smaller distance. Scaling laws in the linear regime illustrate this behavior. The energy gain of a DLWFA scales as $W_D = (\pi/8)(k_{pl}L)a_0^2$, where L is the accelerator length, $k_{pl} = \pi/c\tau_l$, τ_l is the transform-limited pulse duration of the laser, and energies are normalized by $m_e c^2$ throughout. Maximizing the energy gain requires operating at the highest possible

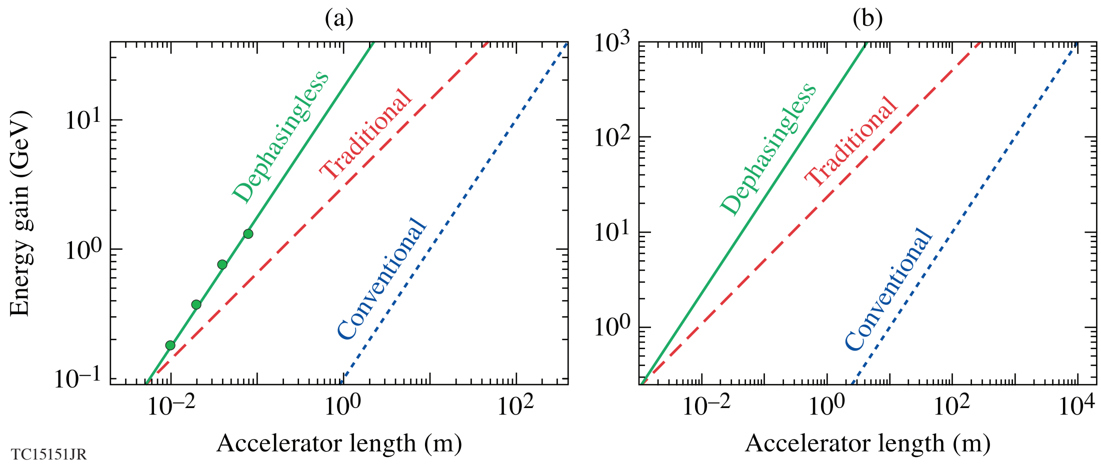

Figure 1
Energy gain of a DLWFA and traditional LWFA in the (a) linear ($a_0 = 0.5$) and (b) nonlinear ($a_0 = 4$) regimes as a function of accelerator length compared with a conventional radio-frequency accelerator. Simulations (green circles) show excellent agreement with the theoretical scaling. The nonlinear DLWFA reaches a TeV energy gain in 4.5 m—40× less distance than a traditional LWFA. The energy gain for the conventional accelerator is determined by the electric-field threshold for material damage, $W_c = E_{thr}L$, where $E_{thr} = 100$ MeV/m. The linear and nonlinear wakefields were driven by a 1-μm laser with $\tau_1 = 30$ fs and $\tau_1 = 15$ fs, respectively.

density, $n_{max} = \pi^2 \alpha_0 m_e / e^2 \tau_1^2$, and increasing the length of the plasma as much as possible. The promise of extending DLWFA to the nonlinear bubble regime—a TeV accelerator in 4.5 m—is illustrated by Fig. 1(b). For a nonlinear DLWFA, $W_D = 1/2\left(k_{pl}L\right)a_0^{1/2}$, where now $k_{pl} \sim a_0^{1/2}/c\tau_1$ in order to match (roughly) half the bubble radius to the transform-limited pulse duration. As before, operating at the highest possible density and increasing the plasma length maximize the energy gain.

The dephasingless wakefield can be excited by a ponderomotive force that travels through the plasma at the speed of light in vacuum over a distance greater than the dephasing length. The novel spatiotemporal technique employed here and depicted in Fig. 2 accomplishes this by using two optics: an axiparabola[3] and a cylindrically symmetric echelon. The axiparabola creates an extended focal region by focusing different radial locations in the near field to different axial locations in the far field. The echelon adjusts the temporal delay of radial locations in the near field to produce the desired ponderomotive or "focal" velocity.

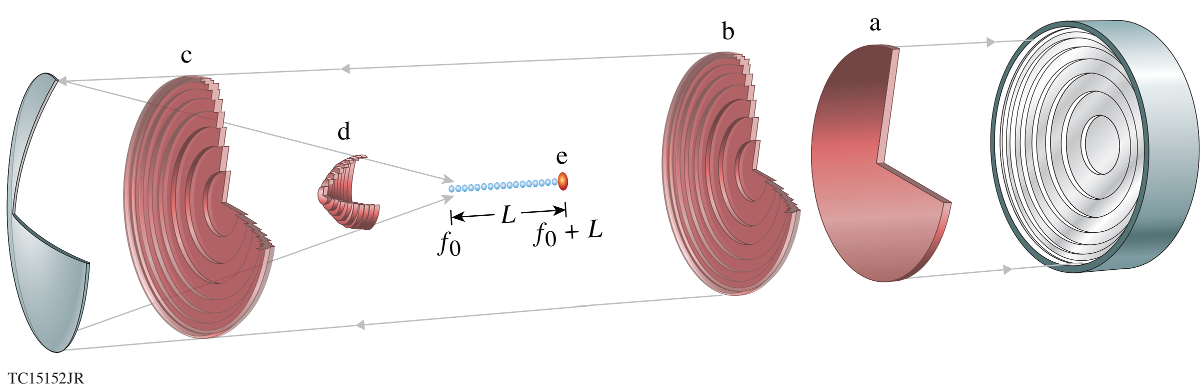

Figure 2
A schematic of the optical configuration enabling the DLWFA. [(a),(b)] The laser pulse first reflects off of a stepped echelon, which imparts the temporal delay required for a focal velocity equal to the speed of light in vacuum without introducing angular dispersion or aberrated focusing. [(c),(d)] After reflecting from the echelon, the pulse encounters the axiparabola, which focuses different rings in the near field to different axial locations in the far field, stretching the region over which the pulse can sustain a high intensity from the initial focus at f_0 to $f_0 + L$. (e) The pulse drives a wakefield at the speed of light in vacuum.

The combined axiparabola/echelon system delivers an ultrashort pulse to each axial location in the focal region without unwanted focusing aberrations and a duration equal to that of the incident pulse.

This material is based upon work supported by the Department of Energy National Nuclear Security Administration under Award Number DE-NA0003856, the University of Rochester, and the New York State Energy Research and Development Authority.

1. T. Tajima and J. M. Dawson, Phys. Rev. Lett. **43**, 267 (1979).
2. E. Esarey, C. B. Schroeder, and W. P. Leemans, Rev. Mod. Phys. **81**, 1229 (2009).
3. S. Smartsev *et al*., Opt. Lett. **44**, 3414 (2019).
4. D. H. Froula *et al*., Nat. Photonics **12**, 262 (2018).

Multibeam Absolute Stimulated Raman Scattering

R. K. Follett,[1] J. G. Shaw,[1] J. F. Myatt,[2] D. H. Froula,[1] and J. P. Palastro[1]

[1]Laboratory for Laser Energetics, University of Rochester
[2]Department of Electrical and Computer Engineering, University of Alberta

Direct-drive inertial confinement fusion (ICF) uses multiple overlapping laser beams to symmetrically implode a millimeter-scale cryogenic capsule of deuterium–tritium fuel. The on-target laser intensity is limited by laser–plasma instabilities that can scatter the incident laser light away from the target and produce high-energy electrons that preheat and degrade the implosion. The two primary instabilities that generate hot electrons in direct-drive ICF experiments are stimulated Raman scattering (SRS), which is the decay of an electromagnetic wave (EMW) into another EMW and an electron plasma wave (EPW), and two-plasmon decay (TPD), which is the decay of an EMW into two EPW's. Understanding the thresholds for these instabilities is critical for designing ICF implosions and developing mitigation strategies.

In most direct-drive ICF experiments, the intensity of a single laser beam is below the instability threshold for either SRS or TPD. For the case of TPD, numerous experimental and theoretical papers have shown that multiple laser beams can interact with shared EPW's, resulting in the instability being driven with single-beam laser intensities well below the instability threshold.[1–4] In particular, experiments on the OMEGA laser have demonstrated that using the overlapped laser intensity in the threshold formula for a monochromatic plane wave provides a reasonable approximation to the multibeam threshold. In contrast, relatively little work has been done on multibeam SRS because SRS is not typically observed in implosion experiments on the OMEGA laser.

This summary presents 3-D calculations of multibeam absolute SRS thresholds. The results provide an explanation for a number of experimental observations on OMEGA and the National Ignition Facility (NIF) that cannot be understood in terms of single-beam thresholds or shared daughter-wave theories. The multibeam coupling is shown to be weaker for SRS than for TPD, which results in thresholds that are consistent with both the NIF and OMEGA experiments. Additionally, the simulations show that it is generally not a good approximation to use the overlapped intensity in the single-beam threshold formulas to predict multibeam instability thresholds for SRS or TPD because the multibeam coupling is sensitive to the density scale length. Finally, in contrast to the single-beam SRS results, the shared EMW mode driven near the quarter-critical density is found to have a lower threshold than the absolute sidescatter mode that occurs at lower densities.

In inhomogeneous plasmas, TPD and SRS can have both convectively and absolutely unstable modes. Convectively unstable modes undergo finite spatial amplification when propagating across a resonant region.[5] Absolute instability corresponds to one of the daughter waves growing more rapidly than energy is convected out of the resonant region, resulting in temporal growth at a fixed point in space.[6,7] Here we will focus on the absolute form of the instabilities because, for conditions relevant to direct-drive ICF, SRS and TPD typically become absolutely unstable at laser intensities where the convective gains are still modest. There are two situations where energy advects slowly out of the resonant region and the absolute thresholds are minimized: (1) one of the daughter waves propagates nearly perpendicular to the density gradient, and (2) one of the daughter waves has a group velocity near zero, which occurs only near $n_c/4$ for TPD and SRS.

The calculations presented here were performed using the laser-plasma simulation environment (*LPSE*) code.[8] *LPSE* solves the time-enveloped wave equations for the electrostatic and electromagnetic plasma response. The individual evolution equations in *LPSE* are linearized, but the coupling between the electrostatic and electromagnetic response leads to nonlinearity. Thresholds are determined by initially bounding the threshold and then iteratively running *LPSE* to narrow the threshold bounds until acceptable accuracy is achieved. The equations that were solved and the technique used to calculate thresholds are discussed in detail in Ref. 9. Unless otherwise specified, the simulations used a linear density gradient from n_e / n_c = 0.22 to 0.27, T_e = 2 keV, and $\lambda_0 = 2\pi c/\omega_0$ = 0.351 μm, and cubic grid cells with a side length of 0.074 μm. The grids were 10 μm wide in the transverse directions (perpendicular to the density gradient) with transverse periodic boundary conditions and absorbing longitudinal boundary conditions. All 3-D simulations used six beams with *f*/6.7 phase plates and polarization smoothing incident at 23° relative to and distributed uniformly about a common axis (similar to an OMEGA "hex"). Error bars correspond to the standard deviation from ensembles of calculations with random realizations of beam polarization, phase, and noise seed.

The primary result presented here is the 3-D multibeam absolute instability thresholds for TPD and SRS shown in Fig. 1. The thresholds are normalized to the single-beam thresholds ($I_{\text{thr,SB}}$) (Refs. 6 and 7). The fact that $I_{\text{thr}} / I_{\text{thr,SB}} \approx 1$ for OMEGA-like conditions (L_n = 200 μm, T_e = 2 keV) is consistent with the empirical observation that the TPD threshold can be predicted by using the overlapped intensity in the single-beam threshold formula. However, this is not true in general for TPD or SRS because the multibeam coupling becomes weaker with increasing scale length. Additionally, the multibeam coupling for SRS is weaker than for TPD, which explains why TPD is the predominant instability observed in OMEGA experiments despite the fact that $I_{\text{thr,TPD}} > I_{\text{thr,SRS}}$.

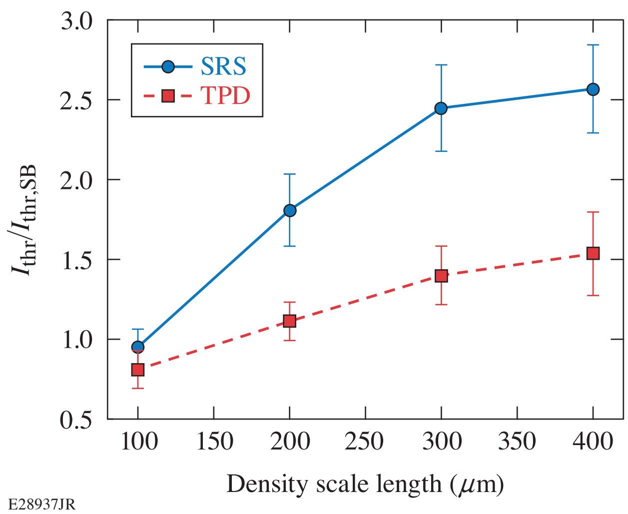

Figure 1
Absolute instability thresholds (normalized to the single-beam thresholds) for SRS (blue circles) and TPD (red squares) near $n_c / 4$ as a function of density scale length using six beams with phase plates and polarization smoothing at T_e = 2 keV. The error bars were obtained from an ensemble of four calculations with random realizations of polarization and phase.

This material is based upon work supported by the Department of Energy National Nuclear Security Administration under Award Number DE-NA0003856, the University of Rochester, and the New York State Energy Research and Development Authority.

1. C. Stoeckl *et al*., Phys. Rev. Lett. **90**, 235002 (2003).
2. D. T. Michel *et al*., Phys. Rev. Lett. **109**, 155007 (2012).
3. J. Zhang *et al*., Phys. Rev. Lett. **113**, 105001 (2014).
4. R. K. Follett *et al*., Phys. Rev. E **91**, 031104(R) (2015).
5. M. N. Rosenbluth, Phys. Rev. Lett. **29**, 565 (1972).

6. B. B. Afeyan and E. A. Williams, Phys. Fluids **28**, 3397 (1985).
7. A. Simon *et al*., Phys. Fluids **26**, 3107 (1983).
8. J. F. Myatt *et al*., J. Comp. Phys. **399**, 108916 (2019).
9. R. K. Follett *et al*., Phys. Plasmas **26**, 062111 (2019).

Hot Raman Amplification

D. Haberberger, A. Davies, J. L. Shaw, R. K. Follett, J. P. Palastro, and D. H. Froula

Laboratory for Laser Energetics, University of Rochester

From its conception at the turn of the 21st century,[1,2] Raman amplification in a plasma has attracted attention from the laser-plasma community for its application to the production of extremely high power laser pulses. While optical parametric chirped-pulse–amplification (OPCPA) technologies have revolutionized high-power laser physics by allowing for a many-orders-of-magnitude increase to the maximum achievable power, another plateau has slowly emerged around the 30-PW level for single beams. Increasing the energy or decreasing the pulse width of these ultrahigh-power lasers requires unfeasibly large compression gratings to avoid damage.[3] As a result, many envisioned applications of high-power lasers remain beyond the intensity frontier.[4] A laser-plasma power amplifier can sustain orders-of-magnitude higher fluences and intensities than solid-state compressor gratings and could provide the technology to expand this frontier. While this promise has sustained interest over the past two decades, experiments have failed to produce a proof-of-principle amplifier scalable to its main application.

The Raman amplification process utilizes a three-wave instability, stimulated Raman scattering (SRS), whereby a short seed pulse at a frequency ω_s counter-propagates with respect to a long energetic pump pulse at a frequency ω_0 in a plasma. The ponderomotive beat wave created by the pump and seed pulses drives an electron plasma wave (EPW) at approximately the plasma frequency $\omega_\mathrm{pe} = \omega_0 - \omega_\mathrm{s}$, where $\omega_\mathrm{pe} = \sqrt{n_\mathrm{e} e^2 / m_\mathrm{e} \varepsilon_0}$, n_e is the electron plasma density, e is the electron charge, m_e is the electron mass, and ε_0 is the permittivity of free space. Under optimal conditions, the pump can transfer a large fraction of its energy to the seed (up to the Manley–Rowe limit $\omega_\mathrm{s}/\omega_0$), thereby amplifying it; however, several phenomena can interrupt this process, depending on where one operates in the vast parameter space that spans pump and seed pulse intensities, seed pulse width, pump wavelength, plasma temperature, and plasma density. Navigating this parameter space is complicated by the lack of a defining metric for scaling a proof-of-principle amplifier to the multi-PW level.

While the signatures of many limiting phenomena have been studied in simulations, the complexities of Raman amplification experiments have inhibited reaching a consensus on how many of, and the extent to which, these phenomena are limiting the performance. This is evidenced by the modest advancement in experiments over two decades, despite many detailed theoretical and simulation studies. Much of the simulation work and all past experiments have focused on amplification in a cold plasma ($\leq$100 eV), where low damping of the SRS instability allows for exponential growth of a weak seed pulse to rapidly reach the efficient pump-depletion regime (Fig. 1, gray-shaded region). In this regime, SRS growing from thermal noise ahead of the seed is often identified as a limiting mechanism,[5,6] but it is typically assumed that it can be detuned with an appropriate amount of pump chirp or plasma density gradient. However, experiments with highly chirped pumps ($\Delta t_\mathrm{stretch} = \Delta t_\mathrm{compressed} > 100$) have yet to surpass an ~3.5% single-stage efficiency.[7] Furthermore, thermal filamentation of the pump has a high gain rate in cold plasmas.[8] While a discussion on filamentation is mostly absent from Raman amplification literature,[9] it can deplete the pump-beam intensity through diffraction and create density perturbations that refract the seed beam, detune the resonant interaction, and imprint modulations on the amplified seed phase front, thereby limiting its focusability.[10]

Here we present a novel high-temperature, efficient Raman amplifier, where deleterious laser instabilities are mitigated. The high temperature increases the intensity threshold for thermal filamentation and generates strong Landau damping of the EPW's, which suppresses SRS growth from thermal noise. The regime takes advantage of quasi-transient amplification,[11] where a sufficiently intense seed pulse allows for amplification, even in conditions where Landau damping exceeds the linear SRS gain. Vlasov simulations were used to demonstrate and define a new regime for proof-of-principle experiments scalable to PW-class amplifiers, where the (1) intensity gains are ≥10, (2) energy transfer efficiencies are ≥30%, and (3) amplified output intensities are ≥100× the pump intensity (Fig. 1, blue-shaded area).

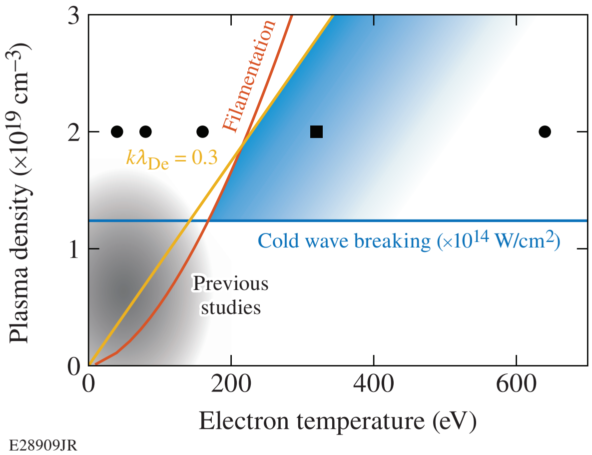

Figure 1
The optimal parameter regime for Raman amplification is shown to be at high temperatures.

At a plasma density of 2×10^{19} cm^{-3}, 1-D Vlasov simulations (ARGOS[12]) at temperatures below 200 eV (black circles in Fig. 1) show strong growth of SRS from noise that depletes the pump pulse before crossing the seed, leaving behind a turbulent EPW spectrum. The square indicates efficient amplification with sufficient gain. Increasing the temperature to 320 eV damps SRS growth from noise driving the interaction into the kinetic regime [$k\lambda_{\mathrm{De}} \geq 0.3$ (Ref. 13), where k is the EPW wave vector and λ_{De} is the Debye length], where a peak efficiency of 55% and intensity amplification factor of 13 were obtained, which is nearly ideal for a next-generation power amplifier. Further increase in the temperature to 650 eV showed a decrease in performance as strong Landau damping and particle trapping inhibit EPW growth. The optimal regime is also shown to be at a plasma temperature above the threshold for thermal filamentation[8] for a pump intensity of 10^{14} W/cm^2. The plasma density resides above the cold wave-breaking limit but not too high so as to not partition a large fraction of the pump energy into the driven EPW. The previous experimental studies on Raman amplification are shown to be plagued with all three limitations described here: wave breaking, SRS growth from noise, and filamentation.

The ultimate goal of Raman amplification is to provide an amplifier for petawatt-scale laser systems; therefore, modest intensity gains ≥10, far below what is often the objective in experiments,[14] are sufficient. Presumably, the seed pulse is created by a state-of-the-art OPCPA system and has a compressed power of the order of 10 PW (Ref. 3) with a pulse width of the order of 10 to 100 fs. The pump pulse, which is of the order of tens of picoseconds, would necessarily have an intensity less than that of the input seed; therefore, a plasma amplifier should require that the amplified seed intensity be a factor of ≥100× larger than the pump intensity. Limiting the energy in the pump to a level attainable in state-of-the-art, solid-state picosecond chirped-pulse–amplification systems requires an energy transfer efficiency of ≥30%. This final criterion is potentially the most difficult to satisfy since it relies on uninhibited pump-beam propagation, no pre-seed depletion of the pump from thermal SRS, and the seed entering the amplifier being intense enough to achieve high-energy transfer—all of which detrimentally affect high-gain amplifiers relying on exponential gain at low temperatures. Here, we have shown through calculations and kinetic simulations that at high temperatures it is expected that all fluid-like limitations are suppressed, while amplification continues in the presence of kinetic limitations such as Landau damping, particle trapping, and warm wave breaking, which are modeled accurately in the Vlasov simulations. The high-power amplifier metrics were satisfied in a 2-mm plasma preheated to 320 eV and seeded strongly at 10^{15} W/cm^2—all experimentally achievable parameters.

This material is based upon work supported by the Department of Energy Office of Science under Award Number DE-FOA-0001820, the Department of Energy National Nuclear Security Administration under Award Number DE-NA0003856, the University of Rochester, and the New York State Energy Research and Development Authority.

1. G. Shvets *et al*., Phys. Rev. Lett. **81**, 4879 (1998).
2. V. M. Malkin, G. Shvets, and N. J. Fisch, Phys. Rev. Lett. **82**, 4448 (1999).
3. C. N. Danson *et al*., High Power Laser Sci. Eng. **7**, e54 (2019).
4. G. Mourou, Rev. Mod. Phys. **91**, 030501 (2019).
5. V. M. Malkin, G. Shvets, and N. J. Fisch, Phys. Rev. Lett. **84**, 1208 (2000).
6. D. S. Clark and N. J. Fisch, Phys. Plasmas **10**, 3363 (2003).
7. J. Ren *et al*., Nat. Phys. **3**, 732 (2007).
8. W. L. Kruer, Comments Plasma Phys. Control. Fusion **9**, 63 (1985).
9. D. Turnbull *et al*., Phys. Plasmas **19**, 073103 (2012).
10. A. A. Solodov, V. M. Malkin, and N. J. Fisch, Phys. Plasmas **10**, 2540 (2003).
11. V. M. Malkin and N. J. Fisch, Phys. Rev. E **80**, 046409 (2009).
12. R. K. Follett *et al*., Phys. Plasmas **26**, 062111 (2019).
13. J. L. Kline *et al*., Phys. Rev. Lett. **94**, 175003 (2005).
14. G. Vieux *et al*., Sci. Rep. **7**, 2399 (2017).

Implementing a Microphysics Model in Hydrodynamic Simulations to Study the Initial Plasma Formation in Dielectric Ablator Materials for Direct-Drive Implosions

A. Kar,[1] S. X. Hu,[1] G. Duchateau,[2] J. Carroll-Nellenback,[1] and P. B. Radha[1]

[1]Laboratory for Laser Energetics, University of Rochester
[2]Université de Bordeaux-CNRS-CEA, Centre Lasers Intenses et Applications

In direct-drive inertial confinement fusion (ICF), a spherical target is irradiated by laser beams to create the necessary conditions for fusion reactions. These targets contain the fusion fuel [deuterium (D) and tritium (T)] inside a plastic (CH) shell. The laser energy on the target causes the plastic to ablate outward like the exhaust of a rocket. This ablation creates a reaction force on the remaining part of the capsule. Ideally, one hopes that this should create a spherically symmetric implosion. However, single-beam speckle (laser imprint) can introduce perturbations that can compromise performance.[1] In fact, the laser energy deposited from a single-beam speckle penetrates through the target nonuniformly. This nonuniformity is intensified by the filamentation of the laser energy that leaves a damage track due to the self-focused laser radiation. These variations act as seeds to Rayleigh–Taylor instability, which grows exponentially. To create a uniform symmetric implosion for ignition, understanding and mitigating this laser-imprint process is important. As the laser beams irradiate the target, the target is ionized and a plasma is created around it. This coronal plasma determines the laser-energy deposition on the target until a critical surface is established and the target becomes opaque to the laser. After this, the subcritical underdense plasma absorbs the laser energy and transfers this energy through the electrons inside the critical surface to the ablation region.

Recently, it has been shown that the initial solid state of the target with specific electronic and optical properties has a notable impact on the subsequent plasma dynamics. It is important to implement a detailed model to understand the solid-to-plasma transition. Therefore, a microphysics model describing the response of the ablator material to the laser-irradiation process on the target has been developed.[2] The microphysics model incorporates a photoionization and impact ionization scheme that describes the transition of the solid ablator into plasma due to laser irradiation. Traditionally, hydrodynamic codes have ignored this detailed transition mechanism from the solid-to-plasma state for the target. The hydrodynamic codes either assume that the material is ionized to start with, and a critical electron density exists initially, or they adopt the "cold-start" method where the laser energy is deposited on the surface of the target to generate a critical surface in an *ad hoc* manner. Both of these strategies are incorrect from a physics perspective. Since radiation-hydrodynamic simulations form an essential component of our understanding of the direct-drive ICF process, it is important to incorporate the microphysics model into the hydrodynamic codes to model the seeds of Rayleigh–Taylor growth including the initial solid state of the target.

In this project, a revised version of the above-mentioned microphysics model[2] has been implemented into the 1-D hydrodynamic code *LILAC*. We demonstrate the implications of the microphysics model in ICF through hydrodynamic simulations for both spherical and planar targets. Unlike the *ad hoc* model, the microphysics model shows laser-energy absorption inside the target over time. Additionally, the energy absorption causes the electron temperature inside the target to rise; subsequently, the pressure inside the target increases. This is consistent with previous observations that the laser beam penetrates through the plastic and deposits energy inside the target since plastic on the outermost layer of the target is transparent to UV laser light of 351-nm wavelength.[3] This phenomenon had not been captured in previous hydrodynamic simulations since the incident laser intensity was restricted to the target surface by creating a critical surface in an *ad hoc* fashion.

This work focuses mainly on plastic or polystyrene ablators since they are commonly used ablator materials for direct-drive ICF targets. CH is a dielectric material with a band gap of 4.05 eV. This makes solid plastic transparent to UV laser light of 351-nm wavelength (or 3.53 eV), the wavelength of TW facilities like OMEGA. Therefore, the laser energy shines through the target in the early stage of laser irradiation. At present, hydrodynamic codes ignore the transparency of plastic to UV light, which is incorrect. To overcome these inaccuracies and develop a physics-based model, a rate equation governing the free-electron density of the electrons in the conduction band has been derived recently.[2] This rate equation as shown in Fig. 1(a) is coupled with a laser-energy–deposition scheme. Based on the laser-energy deposition, the plasma profile and the various physical quantities are determined. This model governs the dynamics of the initial plasma formation from the solid throughout the target during the early stage of the irradiation, until a critical surface is created. During this stage, the laser-energy deposition is mediated by the joule heating mechanism of the electrons in the corona. Once the critical surface forms, the material is ionized and assumed to be in the plasma state. After this time, the microphysics model dominates the plasma profile ahead of the shock front, while the normal *LILAC* method for inverse bremsstrahlung absorption dominates the physics behind the shock front as demonstrated in Fig. 1(b).

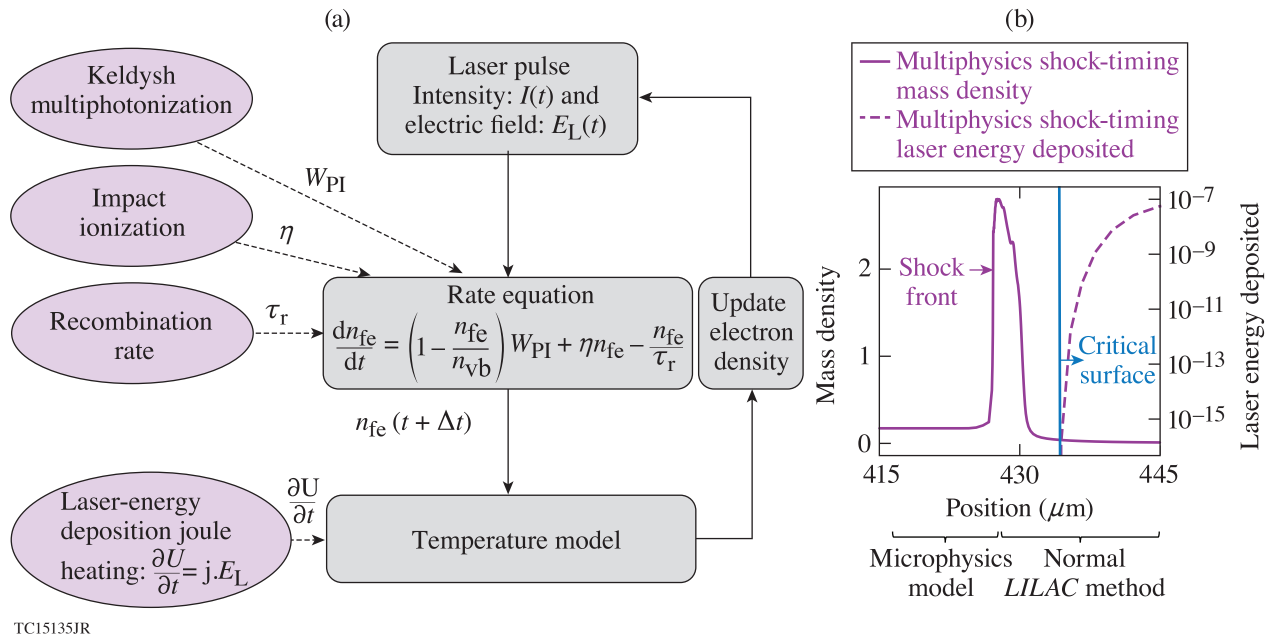

Figure 1
(a) A flowchart with detailed equations, different physical processes, and their implementation sequence inside *LILAC*. (b) An outline of the regions where the microphysics model and the normal *LILAC* method are implemented after the critical surface is formed.

After we implemented this microphysics model into *LILAC*, we examined how it affects hydrodynamic simulations in ICF. The effect of irradiating a solid plastic sphere [Fig. 2(a)] with a picket pulse [Fig. 2(b)] is discussed here. The solid CH sphere is initially transparent to the UV light before the critical surface formation occurs around 81 ps according to simulation. The microphysics model dominates the plasma profile for the entire sphere until the critical surface forms. Beyond that, the microphysics model controls the plasma profile ahead of the shock front. Figure 2(d) shows the plasma profiles in the radially outward direction, 300 μm from the center of the sphere. The plasma profiles are plotted at 75 ps, i.e., before the critical surface forms, at the peak of the picket pulse (200 ps) and at 400 ps, which is the end of the picket pulse. The microphysics model predicts a rise in the electron temperature and pressure before the shock wave travels through the target due to the shinethrough mechanism of the laser light inside the CH.

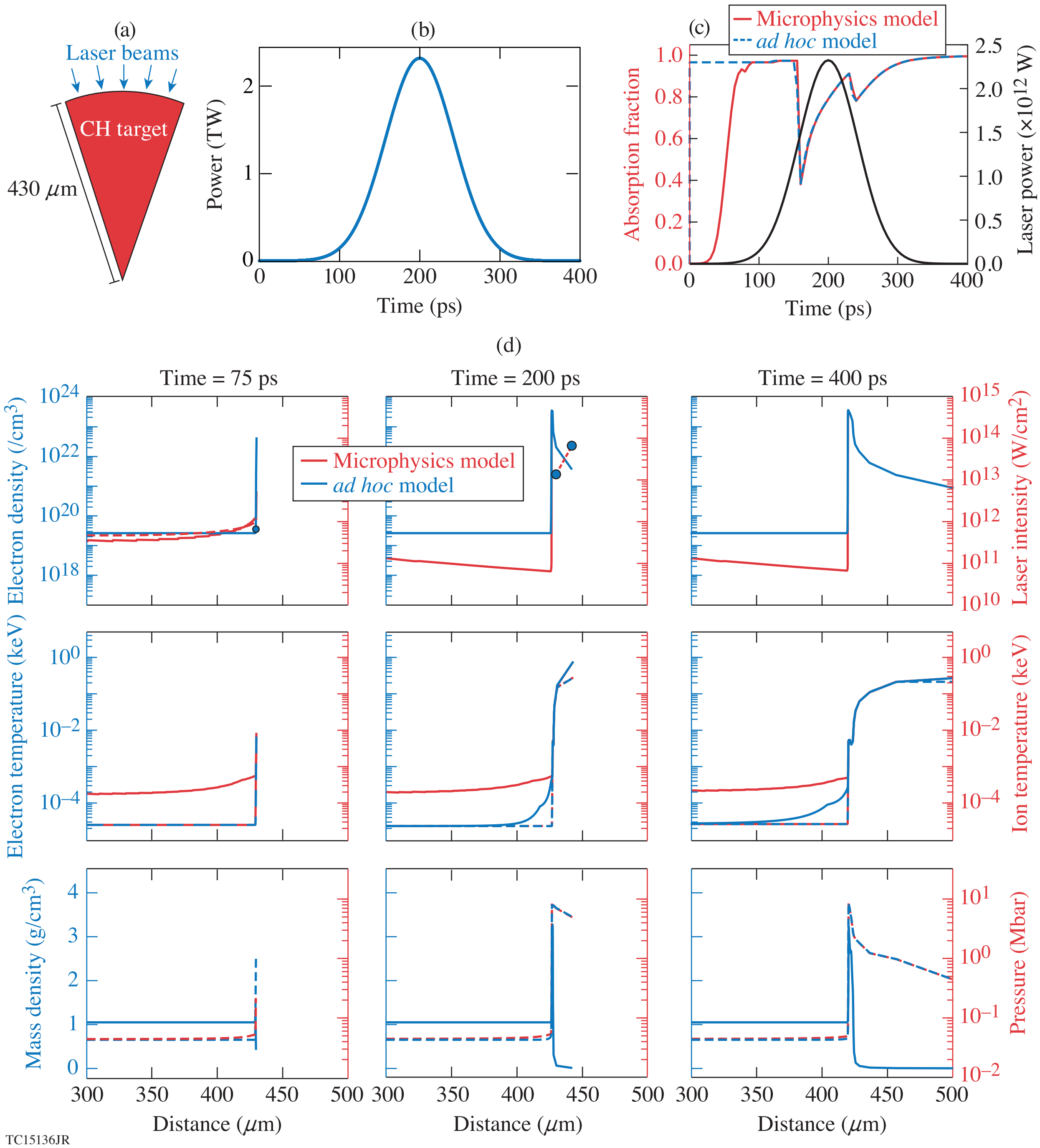

Figure 2
(a) A solid plastic sphere of 430-μm radius is irradiated with (b) a laser pulse of 250 J of energy; (c) the fraction of the incident laser energy absorbed over time. The absorption fraction between the microphysics model and the *ad hoc* model is initially different since the energy deposition is initially restricted to the surface of the target for the *ad hoc* model. Beyond the critical surface formation, the absorption profiles are the same since the plasma profile in the ablation region is controlled by the *ad hoc* model. (d) The plasma profiles from the microphysics model and the *ad hoc* model are plotted in red and blue, respectively. The top row shows the laser intensity deposition profiles (dashed red lines for the microphysics model and solid blue circles for the *ad hoc* model) and the corresponding free-electron density (solid lines). The critical surface formation occurs when the free-electron density rises to 9×10^{21} cm^{-3} for UV light. The middle row shows the rise in the electron temperature (solid lines) predicted by the microphysics model and the ion temperatures (dashed lines). The mass density profile (solid lines) and the difference in the pressure profiles (dashed lines) is evident in the lower row.

The next step is to implement the microphysics model into the 2-D hydrodynamic code *DRACO* for laser-imprint simulations. Perturbations to the ablation pressure as a function of angle due to the target response to laser imprint will be modeled with *DRACO*. Efforts to study the consequences of the microphysics model for a cryogenic implosion are also underway as the material properties of DT gas and DT ice are being investigated. It is necessary to know the band gap, collisional frequency, and recombination rates for these materials to accurately implement the microphysics model.

This material is based upon work supported by the Department of Energy National Nuclear Security Administration under Award Number DE-NA0003856, the University of Rochester, and the New York State Energy Research and Development Authority.

1. R. Ishizaki and K. Nishihara, Phys. Rev. Lett. **78**, 1920 (1997).
2. G. Duchateau *et al.*, Phys. Rev. E **100**, 033201 (2019).
3. D. H. Edgell *et al.*, Phys. Plasmas **15**, 092704 (2008).

Extreme Atomic Physics: *Interspecies Radiative Transition* in Warm and Superdense Plasma Mixtures

S. X. Hu,[1] V. V. Karasiev,[1] V. Recoules,[2] P. M. Nilson,[1] N. Brouwer,[2] and M. Torrent[2]

[1]Laboratory for Laser Energetics, University of Rochester
[2]CEA, DAM, DIF

Superdense plasmas, having mass densities ranging from tens to over millions of grams per cubic centimeter, widely exist in planetary interiors and astrophysical objects such as brown-dwarf cores and white dwarfs. How atoms, the fundamental "building blocks" of matter, behave under such extreme density conditions is not yet well understood, even in single-species plasmas. Seeking a deeper understanding of atomic physics in superdense plasmas is now becoming possible because these extreme states of matter can be created and probed in the laboratory by using powerful lasers or pulsed-power machines. Here, we have applied the thermal density functional theory (DFT) to investigate the radiation spectra of superdense iron–zinc (Fe–Zn) plasma mixtures at mass densities of $\rho = 250$ to 2000 g/cm^3 and temperatures of $kT = 50$ to 100 eV, accessible by imploding double-shell targets. Our *ab initio* calculations reveal two *new* and uniquely extreme atomic physics phenomena—firstly, an *interspecies radiative transition* (IRT); and, secondly, the *breaking down of the dipole-selection rule* for radiative transitions in isolated atoms. Our *first-principles* DFT calculations predict that for superdense plasma mixtures, both interatomic radiative transitions and dipole-forbidden intra-atomic transitions can become comparable to the normal intra-atomic K_α-emission signal because of the superdense environment.

For a warm and superdense Fe–Zn plasma of ρ = 1000 g/cm^3 and kT = 50 eV with 1*s* vacancies of both Fe and Zn ions, the calculated emission coefficient as a function of photon energy is shown by the solid red line in Fig. 1. To identify the IRT fea-

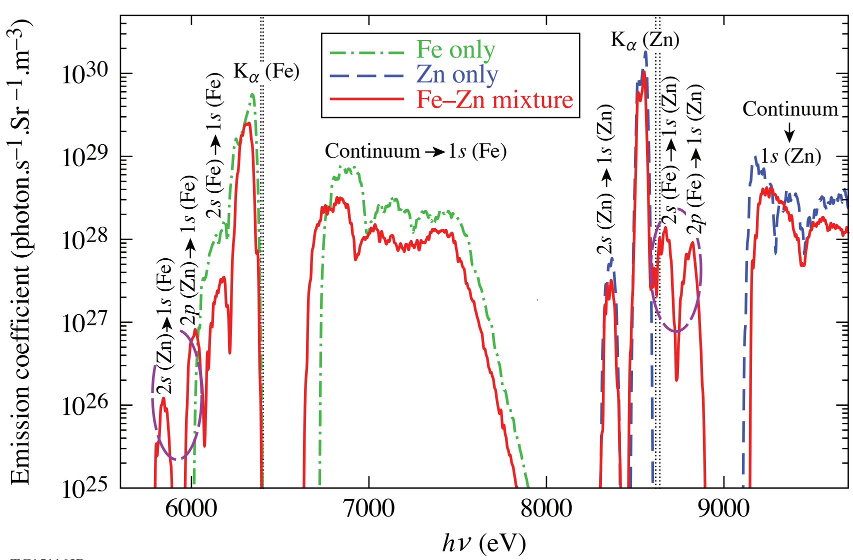

Figure 1
The emission spectra of superdense plasmas of Fe only, Zn only, and a Fe–Zn mixture having 1*s* vacancy at ρ = 1000 g/cm^3 and kT = 50 eV, calculated by DFT using *ABINIT*.

tures, we also plotted the spectra of single-species Fe (dashed–dotted green line) and Zn (dashed blue line) plasmas in Fig. 1, respectively. Again, these pure plasmas have the same density and temperature conditions as those of the Fe–Zn mixture. From Fig. 1, one can clearly see that four new spectral peaks appear in the superdense Fe–Zn plasma mixtures (highlighted by the dashed ellipse): the two new emission lines located at $h\nu \approx 8666$ eV and $h\nu \approx 8816$ eV correspond to transitions from the $2s$ and $2p$ states of the Fe ion to the $1s$ hole of the Zn ion, while the other two new peaks at $h\nu \approx 5838$ eV and $h\nu \approx 6012$ eV belong to radiative transitions of $2s/2p$ electrons of the Zn ion to the $1s$ vacancy of Fe. Besides these new interatomic K_α emissions, the dominant intra-atomic K_α lines for each species are, of course, present in the emission spectra in Fig. 1. The vertical dotted black lines mark the normal intra-atomic K_α locations of ambient Fe and Zn, respectively. The red shift of the intra-atomic K_α line is caused by the increased electron screening resulting from the dense plasma environment. In addition, the intra-atomic $2s \longrightarrow 1s$ transitions for each species, although being about three orders of magnitude weaker than the normal intra-atomic K_α lines, also appear as a consequence of the breaking down of the dipole-selection rule due to the density-induced distortion of $2s$ states. Finally, the continuum emissions from free electrons filling $1s$ holes of Fe and Zn ions are also present in the emission spectra, as expected (shown by Fig. 1).

Interspecies and dipole-forbidden radiative transitions were not previously considered for emissivity/opacity calculations in extremely dense plasma mixtures, directly impacting our understanding of astrophysical objects and, more generally, of the extreme atomic physics that can occur in plasma mixtures at very high energy densities.

This material is based upon work supported by the Department of Energy National Nuclear Security Administration under Award Number DE-NA0003856, the University of Rochester, and the New York State Energy Research and Development Authority.

Stimulated Raman Scattering Mechanisms and Scaling Behavior in Planar Direct-Drive Experiments at the National Ignition Facility

M. J. Rosenberg,[1] A. A. Solodov,[1] W. Seka,[1] R. K. Follett,[1] J. F. Myatt,[2] A. V. Maximov,[1] C, Ren,[3] S. Cao,[3] P. Michel,[4] M. Hohenberger,[4] J. P. Palastro,[1] C. Goyon,[4] T. Chapman,[4] J. E. Ralph,[4] J. D. Moody,[4] R. H. H. Scott,[5] K. Glize,[5] and S. P. Regan[1]

[1]Laboratory for Laser Energetics, University of Rochester
[2]Department of Electrical and Computer Engineering, University of Alberta
[3]Department of Mechanical Engineering, University of Rochester
[4]Lawrence Livermore National Laboratory
[5]Central Laser Facility, STFC Rutherford Appleton Laboratory

Direct-drive inertial confinement fusion implosions may be susceptible to preheat by hot electrons generated by laser–plasma instabilities. Stimulated Raman scattering (SRS), which occurs at densities around and below the quarter-critical density of the laser $\left[n_e = n_c/4\right.$, where n_e is the electron density and n_c is the critical density for the laser wavelength λ_0 (in μm), with $\left.n_c \approx 1.1 \times 10^{21}\, \lambda_0^{-2} \mathrm{cm}^{-3}\right]$, has been observed to be a prominent hot-electron–generating instability in direct-drive experiments at the National Ignition Facility (NIF).[1]

Planar-geometry experiments were conducted on the NIF to elucidate the SRS mechanisms present in direct-drive ignition-scale plasmas, intensity thresholds for SRS, and the scaling of SRS with laser intensity for different laser beam angles of incidence. These experiments were designed to achieve plasma conditions relevant to direct-drive–ignition designs, with density scale lengths $L_n \sim 600\ \mu$m, electron temperatures $T_e \sim 4.5$ keV, and laser intensities at $n_c/4$ between $I_{n_c/4} \sim 4 \times 10^{14}$ and 1.3×10^{15} W/cm^2.

Figure 1 shows the experimental setup, simulated quarter-critical plasma conditions by the 2-D radiation-hydrodynamic code *DRACO*, and time-resolved SRS spectral data collected along the target normal. As shown in Fig. 1(a), the experiment used 32 beams (eight "quads") at incidence angles <35° on a CH ablator and a linearly ramped laser pulse to reach simulated conditions at $n_c/4$ of up to $I_{n_c/4} \sim 8.5 \times 10^{14}$ W/cm^2, $L_n \sim 580\ \mu$m, and $T_e \sim 4.0$ keV [Fig. 1(b)]. The scattered-light spectrum [Fig. 1(c)] shows two features: a narrow feature at around 710 nm corresponding to half-harmonic $\left(\omega_0/2\right)$ emission and a broader feature between 600 and 660 nm. The $\omega_0/2$ feature corresponds to an absolute SRS instability at $n_c/4$, while the lower-wavelength feature is generated by SRS in the underdense $\left(<n_c/4\right)$ region.[1] Lineouts of each feature reveal differences in the time histories of the underlying instabilities. While the $\omega_0/2$ feature increases nearly linearly with laser intensity [Fig. 1(d)], signifying a saturated absolute SRS instability, the underdense SRS feature increases exponentially with laser intensity [Fig. 1(e)], suggesting that this instability is observed in its linear convective stage.

Additional experiments were conducted with the planar target oriented normal to the NIF polar axis. In these experiments, the target was irradiated in cylindrical symmetry by laser beams at well-defined angles of incidence, either 23° and 30° ("inner beams") or 45° and 50° ("outer beams"). SRS was diagnosed by optical streaked spectrometers at viewing angles of 23° and 50°, revealing different SRS mechanisms, all from the underdense region. As previously observed,[1] SRS was detected at each viewing angle for each of the inner-beam and outer-beam laser drives. The observations at 50°, whether generated by inner or outer beams, are interpreted as tangential sidescatter, with the SRS-scattered light propagating parallel to density contours before refracting and propagating out of the plasma.[2] The observations at 23° correspond to either backscattered or sidescattered SRS light.

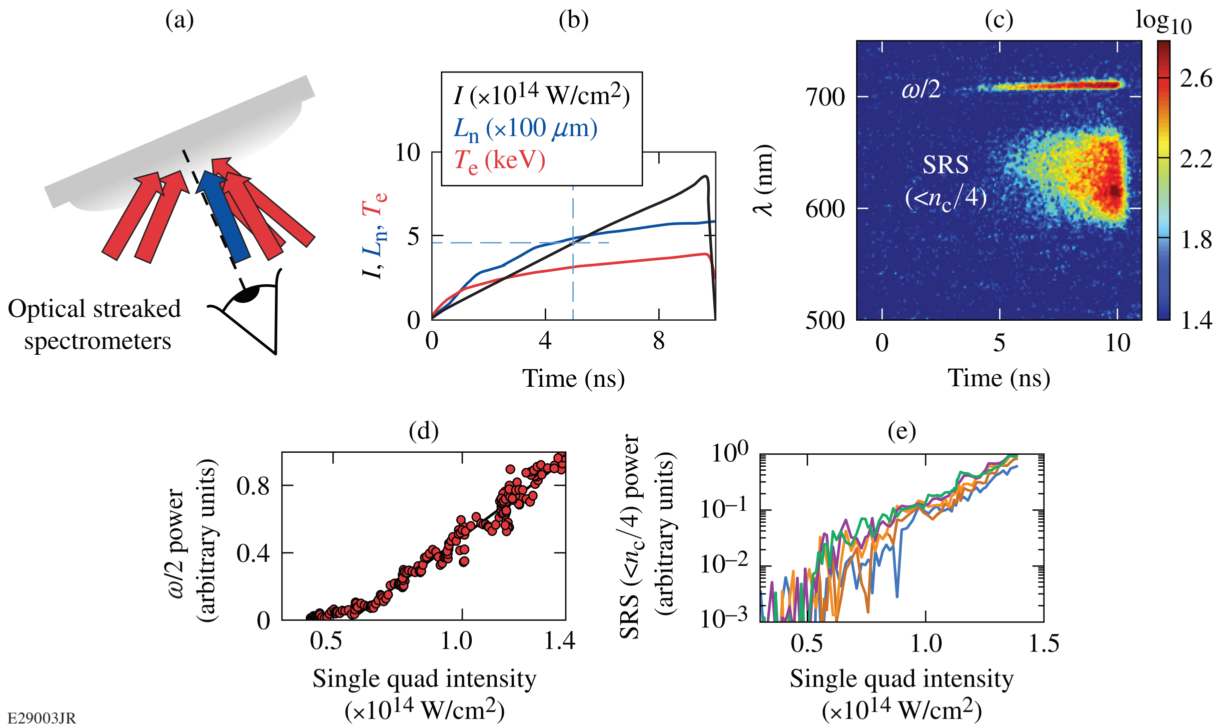

Figure 1
(a) Experimental geometry and SRS observations along the target normal using a ramped laser pulse. The (b) simulated total overlapped laser intensity (black line), density scale length (blue line), and electron temperature (red line) at $n_c/4$ increased continuously with time, corresponding to (c) the time-resolved optical spectrum. The power in each spectral component [(d) $\omega/2$ and (e) sub-$n_c/4$ SRS, with the various colored lines representing the signal integrated over different 5-nm-wide wavelength bands] as a function of the single-quad intensity at $n_c/4$ shows scaling behavior and intensity thresholds.

Within this configuration, several experiments were conducted in which particular "quads" (groupings of four NIF beams) were toggled on or off to elucidate single-quad or multi-quad contributions to the SRS signal. A strong correlation was observed between quads at 50° and the SRS observation at that location, strongly indicating a single-quad tangential sidescatter of outer beams. A moderate correlation was observed between quads at 23° and SRS observations at 50° along the same azimuthal angle, while a stronger correlation was observed between two neighboring inner quads and the 50° SRS measurement. The latter may indicate a multiple-quad effect.[3] Other SRS observations at 23°, as well as along the target normal, did not show strong single-quad contributions and therefore are inferred to be generated by many beams.

Notably, in addition to the underdense SRS observed along target normal, the underdense SRS at other viewing locations, corresponding to sidescatter as well as backscatter, all appear to have a near-exponential dependence on laser intensity in experiments with a linear-ramp laser pulse.

Hard x-ray (HXR) measurements were also obtained in order to relate the SRS observations to hot-electron production. Figure 2 shows HXR and SRS data obtained on experiments with either linear-ramp laser pulses or flattop laser pulses driven by inner beams [Fig. 2(c)]. The linear-ramp pulse experiments show a correlation of time-resolved HXR signal and SRS signal from several viewing locations representing scattered light from the underdense region [Fig. 2(a)]. The HXR emission scales nearly exponentially with time—or with laser intensity—on ramp-pulse experiments [Figs. 2(a) and 2(b)], similar to what was observed for the underdense SRS-scattered light as shown in Fig. 1(e) and at other viewing angles. In addition, a time-integrated SRS signal

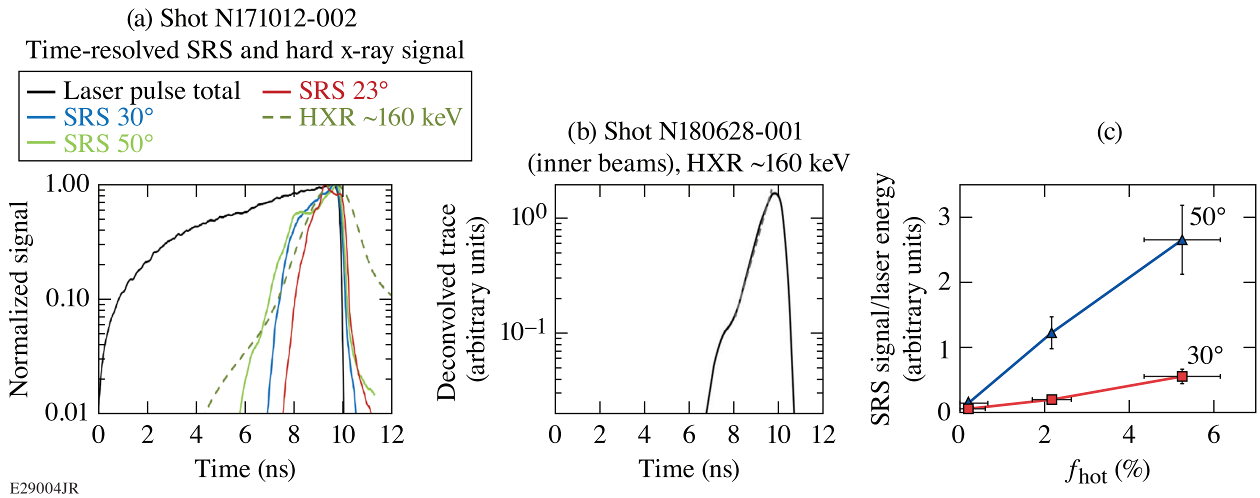

Figure 2
SRS and HXR data from [(a),(b)] ramp pulse and (c) flattop-pulse experiments driven by inner beams. (a) The normalized time-resolved SRS signals from various viewing angles have a time history similar to 160-keV HXR's. (b) Another ramp-pulse experiment produced a HXR signal that is nearly exponential with time (or with laser intensity). (c) Time-integrated SRS signals at 50° and 30° viewing angles, representing SRS from the underdense region, are directly proportional to the fraction of laser energy converted to hot electrons, indicating a correlation.

measured at 30° and 50° from target normal is directly proportional to the measured fraction of laser energy converted to hot electrons (f_{hot}) [Fig. 2(c)]. The correlation of HXR measurements and these SRS observations suggests a connection between SRS in the underdense region and hot-electron production.

Although further modeling is needed to explain the precise SRS mechanism by which hot electrons are generated, these results can be used to guide direct-drive–ignition designs in which hot-electron preheat coupled to the inner layer of the imploding target must be kept below ~0.1%.

This material is based upon work supported by the Department of Energy National Nuclear Security Administration under Award Number DE-NA0003856, the University of Rochester, and the New York State Energy Research and Development Authority.

1. M. J. Rosenberg *et al.*, Phys. Rev. Lett. **120**, 055001 (2018).

2. P. Michel *et al.*, Phys. Rev. E **99**, 033203 (2019).

3. S. Depierreux *et al.*, Phys. Rev. Lett. **117**, 235002 (2016).

Modeling Magnetic Confinement of a Laser-Generated Plasma in Cylindrical Geometry Leading to Disk-Shaped Structures

L. S. Leal,[1,2] A. V. Maximov,[1,3] R. Betti,[1,2,3] A. B. Sefkow,[1,2,3] and V. V. Ivanov[4]

[1]Laboratory for Laser Energetics, University of Rochester
[2]Department of Physics & Astronomy, University of Rochester
[3]Department of Mechanical Engineering, University of Rochester
[4]Department of Physics, University of Nevada, Reno

Strong magnetic fields can play a pivotal role in the dynamics of a plasma.[1,2] Understanding the interactions in plasmas in strong fields is important for many areas of plasma physics, ranging from basic and applied plasma physics to astrophysics, controlled fusion, and *Z*-pinch experiments.[3–8] Understanding plasma dynamics and transport in laser-produced plasmas in strong external fields has become an important area of research in inertial confinement fusion after the demonstration of fusion yield enhancement in laser-driven implosions[9] and the most recent demonstrations of the magnetized liner inertial fusion concepts at Sandia National Laboratories.[10,11] Recent work from Lawrence Livermore National Laboratory[12] showed that by increasing the initial seed field to 60 T or 0.6 MG, the compressed field in National Ignition Facility implosions can reach hundreds of megagauss, reduce heat losses, and even confine the alpha particles. For an effective alpha-particle confinement, the compressed B field must be large enough that the thermal and magnetic pressures become comparable, as is the case in experiments of laser-generated plasmas in strong external magnetic fields.[13,14] Modeling of these experiments can lead to a broader understanding of plasma dynamics and transport. Recent experiments at the University of Nevada, Reno[13,14] have shown that laser-produced plasmas in strong magnetic fields generated by pulsed-power machines form localized structures that have unique plasma characteristics and exist for many nanoseconds after the end of the laser pulse. The experiments produced a plasma by shining a laser with a 1.056-μm wavelength and 0.8-ns pulse duration at an intensity of ~3×10^{15} W/cm^2 with a 30-μm spot size on an Al rod. The rod had a 1-mm diameter and 0.8 to 1 MA of current driven by the Zebra pulsed-power machine. A low-density, cold plasma was initially formed on the rod surface from the current and generated a magnetic field that was measured through Faraday probes to be 200 to 300 T. The laser ablated plasma of the rod surface and within nanoseconds after the laser pulse, the plasma formed a disk-shaped structure that expanded in the radial direction. Measured values using laser probing and x-ray spectroscopy showed the plasma had electron densities of the order of $n_\mathrm{e} \sim 10^{18}$ cm^{-3}, average electron temperatures $T_\mathrm{e} \sim 400$ eV, and an expansion velocity of $v \sim 250$ km/s. In modeling this interaction, further insight can be gained of the magnetohydrodynamic effects in laser-generated plasmas in strong magnetic fields.

A series of *HYDRA* simulations are discussed here with parameters similar to the conditions of experiments at the Zebra facility.[13] Current driven through an Al rod generates azimuthal $B_\theta \sim 3$ MG at the surface of the rod. In experiments the current pulse time is hundreds of nanoseconds—much longer than the laser pulse and interactions leading to the generation of the disk. In the simulations, the external magnetic field is set by the boundary conditions generating the current in the rod and the 3-MG field at the surface of the rod is similar to what was detected in experiments. A laser with wavelength $\lambda = 1.057$ μm illuminates the rod surface once the magnetic field has been initialized, ablating plasma with a pulse duration of 0.8 ns. The laser is injected through the *HYDRA* laser ray-trace package and enters from the large radius boundary in simulations. The simulations are 2-D with symmetry around the vertical axis. Without an external magnetic field, the ablated plasma is ejected in all directions away from the target rod. The presence of the MG magnetic field greatly affects the dynamics of the ablated plasma. The structure formed by the ablated plasma is well confined in the axial direction but continues to move in the radial direction at velocities of 300 to 600 km/s. Figure 1 compares simulation results at 3 ns after the end of the laser pulse for the plasma generated by

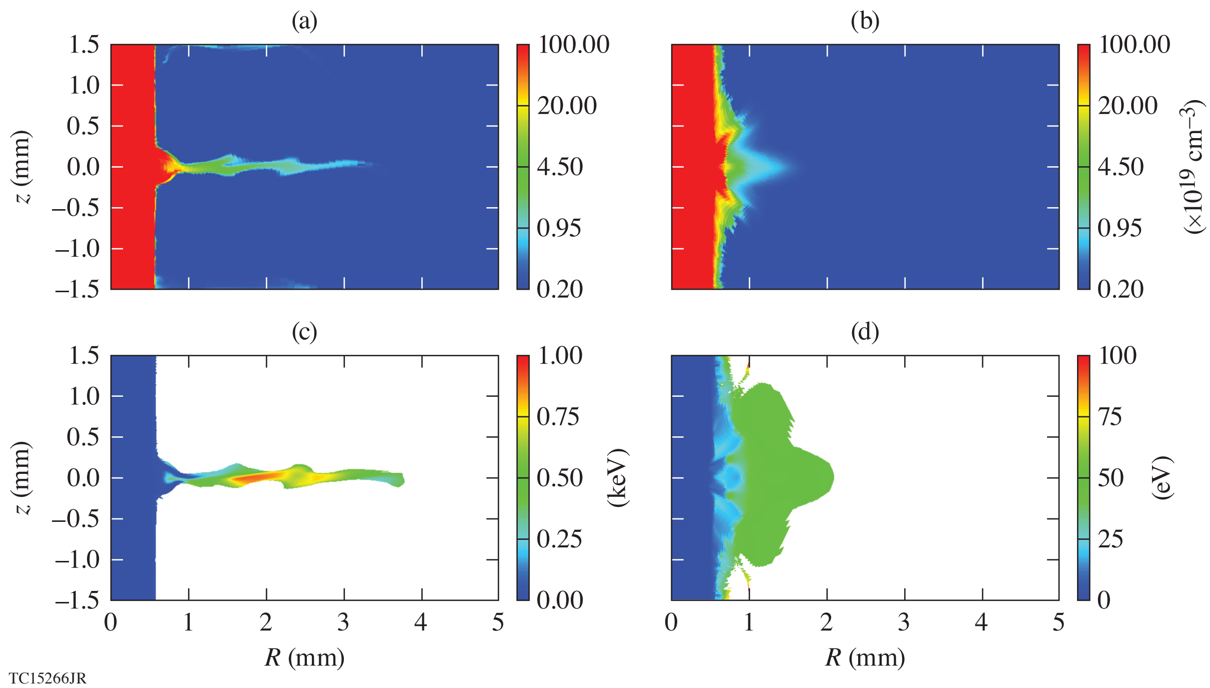

Figure 1
Electron density and temperature of laser-ablated plasma in the case [(a) and (c)] with and [(b) and (d)] without the external magnetic field, respectively, at 3 ns after the end of the laser pulse.

the laser for two cases: with current flowing through the rod (generating the 3-MG field) and without current flowing through the rod. The electron density and temperature in Fig. 1 illustrate the overall structure of the expanding plasma. For the plot of electron temperature, only the area of the ablated plasma is shown, not the "vacuum" region, which in simulations is a very low density plasma that does not affect the overall expansion of the disk plasma but can exhibit numerical noise. It can be seen from Fig. 1(a) that the plasma in the disk is underdense to the laser in the range of $n_e \sim 10^{18}$ to 10^{19} cm^{-3} but more dense and much more extended than in the unmagnetized case [Fig. 1(b)]. The plasma is fully ionized and is contained within the width of 0.1 to 0.2 mm. This collimated plasma structure, when rotated around the axis, would resemble a disk. The plasma of the disk is also much hotter than the plasma without an applied external B field. A feature seen in experiments is the presence of rings in the disk similar to Fig. 1(a) if it is rotated azimuthally.

The 2-D modeling is an important step in comparing with experimental results. The motion of the plasma following the field lines around the rod appears to be a 3-D effect of the plasma being pinched in the axial direction and leading to spreading in the azimuthal direction. The external magnetic field in the MG regime is strong enough to apply magnetic pressure that reshapes the structure of the ablated plasma, as seen in both experiment and simulation. Simulations are able to demonstrate that the strong external magnetic field outside the formed plasma provides plasma confinement in the axial direction. Interaction of laser-generated fields with the external magnetic fields leads to asymmetry of the magnetic field inside the disk. As we have shown, applying strong external fields to laser-generated plasmas leads to complex plasma structures that can be used to study fundamental plasma physics and astrophysical phenomena. The large variation in the Hall parameter also allows one to study how plasma transport properties vary as weakly magnetized plasmas transition into strongly magnetized plasmas.

This material is based upon work supported by the Department of Energy under award number DOE Grant DE-SC0016500, Department of Energy National Nuclear Security Administration under Award Number DE-NA0003856, the University of Rochester, and the New York State Energy Research and Development Authority.

1. H. Alfvén, Nature **150**, 405 (1942).

2. J. P. Knauer *et al*., Phys. Plasmas **17**, 056318 (2010).

3. O. V. Gotchev *et al*., Phys. Rev. Lett. **103**, 215004 (2009).

4. D. B. Sinars *et al*., Phys. Rev. Lett. **105**, 185001 (2010).

5. A. Arefiev, T. Toncian, and G. Fiksel, New J. Phys. **18**, 105011 (2016).

6. A. B. Sefkow *et al*., Phys. Plasmas **21**, 072711 (2014).

7. M. Hohenberger *et al*., Phys. Plasmas **19**, 056306 (2012).

8. Y. Sentoku *et al*., J. Phys. IV France **133**, 521 (2006).

9. P. Y. Chang *et al*., Phys. Rev. Lett. **107**, 035006 (2011).

10. S. A. Slutz and R. A. Vesey, Phys. Rev. Lett. **108**, 025003 (2012).

11. M. R. Gomez *et al*., Phys. Rev. Lett. **113**, 155003 (2014).

12. L. J. Perkins *et al*., Phys. Plasmas **24**, 062708 (2017).

13. V. V. Ivanov *et al*., Plasma Phys. Control. Fusion **59**, 085008 (2017).

14. V. V. Ivanov *et al*., Phys. Plasmas **26**, 062707 (2019).

Axial Proton Probing of Magnetic and Electric Fields Inside Laser-Driven Coils

J. L. Peebles, J. R. Davies, D. H. Barnak, T. Cracium, M. J. Bonino, and R. Betti

Laboratory for Laser Energetics, University of Rochester

The capability of generating strong, localized, and applicable magnetic fields provides an excellent opportunity in high-energy-density (HED) research environments. Such a tool would have applications in magnetizing HED plasmas,[1,2] field compression leading to fusion yield enhancement,[3–7] particle collimation,[8,9] and magnetized shock physics.[10–14] The laser-driven coil (LDC) has been proposed several times in previous decades[15–27] as a method to generate kilotesla (kT) magnitude fields in a small volume, with the precision of a laser system. Fields ranging from 0.001 T (Ref. 20) to over 1 kT (Ref. 15) have been inferred from previous experiments. Since the generation of these fields can be precisely tuned using the geometry of a thin metal target, LDC's can potentially provide a substantial benefit over traditional pulsed-power, magnetic-field–generation mechanisms[28,29] because they are easier to place in close proximity to experiments and are "triggered" precisely by a laser. LDC's usually consist of two parallel plates connected with a wire loop advantageously shaped to generate a field. A laser passes through a hole in one of the plates and ejects hot electrons from one plate to the other. The charge displacement then draws a return current through the loop from the source plate on the other side, which may also become negatively charged after capturing some electrons from the interaction.[15–27]

Axial Proton Probing and Motivation

The method for diagnosing fields inside the region of interest of an LDC in this summary is "axial proton probing." High-energy protons travel axially through the loop rather than transversely. Since magnetic-field lines must always form a closed loop, a significant axial field will generate a radial field. This radial field will induce a deflection of protons traveling in the axial direction. Upon initial inspection, it would appear that the protons should not see any net deflection at all from a radial field; any deflection of a proton incurred by the radial field will be reversed upon encountering the opposing radial field when leaving the coil. This approximation only holds true, however, in the paraxial approximation. In reality, a proton will be deflected significantly by the initial field, leading to a rotation as it passes through the coil. It will then be returned (approximately) to its original velocity vector after leaving, resulting in a measurable rotational shift as seen in the synthetic radiograph in Fig. 1(a). There are also two second-order effects: the field encountered by the exiting proton is not necessarily the opposite of the field it encountered when it entered and the velocity vector of the proton leaving is not identical to when it entered. Therefore, in theory, a magnetic field generated by a current traveling in the loop will induce a rotation in the proton image when using a spatial fiducial. The estimated mesh rotation, calculated from multiple simulated loops with only a magnetic field, is described by Eq. (1):

$$\theta^{\circ}_{\mathrm{rot}} \approx \frac{0.23 I_{\mathrm{loop}} r^{-0.27}}{\sqrt{E_{\mathrm{p}}}}, \tag{1}$$

where r is the radius of the loop, I_{loop} is the current, and the deflection depends inversely on the square root of the proton energy E_{p}, as expected. The anticipated deflection of protons due to the expected electric field is shown in Fig. 1(b), which shows a clear focusing and stretching effect on the mesh fiducial. The clear difference in the deflection effect demonstrates that this method of proton radiography is able to distinguish deflection contributions from radial electric and magnetic fields.

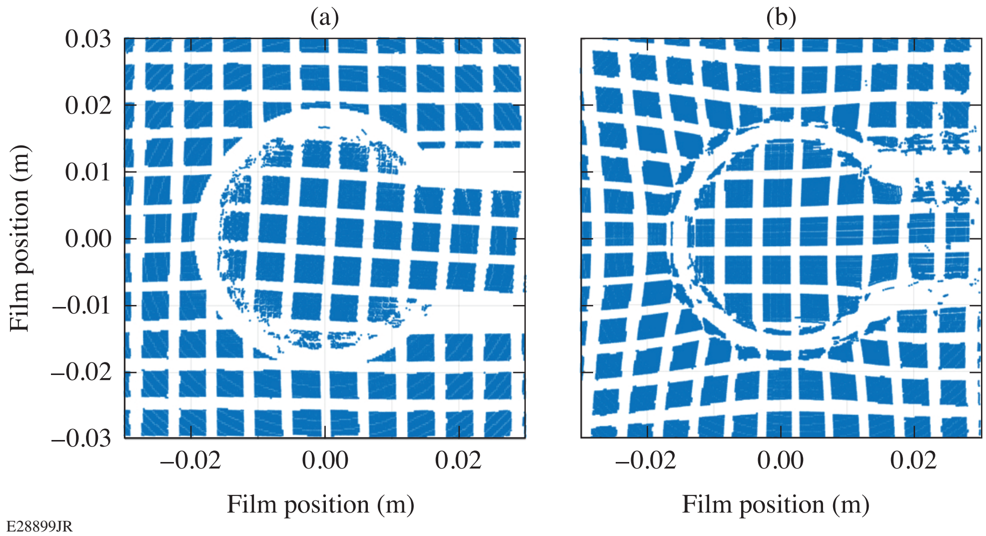

Figure 1
(a) A synthetic axial radiograph (magnification ~16) demonstrates the rotation of the mesh fiducial due to the radial magnetic field. A 90-kA current corresponding to 80 T at the center of the loop was applied along the wire surfaces. (b) A synthetic radiograph demonstrates the pinching of the mesh due to an electric field generated by displacing electrons from the wire.

Axial proton probing also provides more-comprehensive information at the center of the coil regarding plasma density. Any sheath structure, plasma jets, or significant plasma density will be detectable in the axial probe, whereas coil material will always block a transverse probe. Information about conditions inside the coil is of interest for any experiment that would use a LDC to magnetize a target inside of it. Since creating synthetic radiographs for comparison requires several assumptions on location of charge and current, the information of sheath structure position is extremely helpful in reducing parameter space. Since deflections are relatively weaker in the axial proton probing case, more use can be made of the mesh fiducial. Each mesh line and each grid point are effective measurements of the fields in the system, providing hundreds of data points with each shot rather than one or two, as is the case with transverse proton probing.

Experimental Setup

To verify the effectiveness of the axial proton probe, experiments were conducted on the OMEGA EP Laser System. The goal of these experiments was not to generate the field with the highest magnitude, rather it was to generate a field that could be comprehensively diagnosed with the axial probe. Therefore a coil with a comparatively large radius (750 μm) was chosen due to concerns that with high magnitude fields and potential plasma blowoff, protons could be attenuated when passing through the coil. As shown in Fig. 1, an anticipated field of 80 T would result in a modest rotation that would be quantifiable. Furthermore, current along the parallel wires would induce a "twist" across the parallel wires, which could be detected. The experiment had an additional goal of testing a single-plate coil design, similar to experiments performed by Zhu *et al.*[24] The single-plate geometry enhances the feasibility of fielding the LDC as a magnetic-field generator on other experimental platforms such as magnetized inertial confinement fusion and magnetized shocks.

To achieve these goals, experiments were performed with multiple setups and coil types as shown in Fig. 2. Targets consisted of a laser-cut, 2-mm-diam, 0.1-mm-thick copper disk driven by a 1-ns, 1.25-kJ, 351-nm long-pulse beam with a nominal intensity of 6×10^{15} W/cm^2. The disk was attached to a 750-μm-radius coil of the same material via a 2-mm stretch of wire with a 0.1×0.1-mm-sq cross section. The coil would then either return to a second plate placed in front of the first with a 1.2-mm hole placed for the driving beam (double-plate configuration) or connect to a flag with near mass equivalence placed away from the driven plate (single-plate configuration). The double-plate configuration tested two plate separations: 0.5 mm and 0.8 mm. The targets were constructed by cutting a single piece out of a copper foil and then subsequently shaping the target around a custom fixture. The target stalk (made of silicon carbide) was attached to either the flag or the undriven plate in order to remove the stalk as a potential source of electrons.

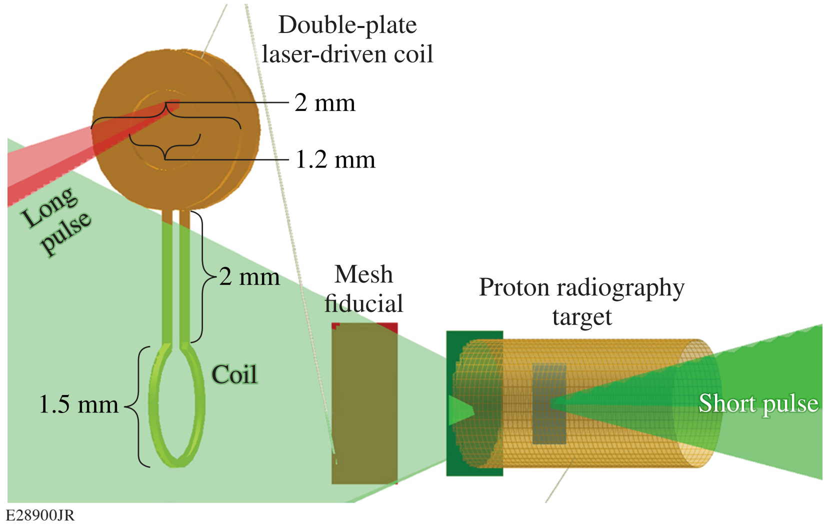

Figure 2
Experimental setup for the double-plate experiments. An OMEGA EP long-pulse beam passes through a front plate and hits the driving plate, which induces a current in the loop. The loop is probed with protons generated by a proton radiography target with a mesh fiducial placed halfway between the source and target.

The coil was probed using a short-pulse–based, proton radiography setup. A 0.7-ps, 300- to 500-J beam, with a nominal intensity of 0.6 to 1×10^{20} W/cm^2, was incident on a copper foil placed in a shielded tube 5 mm from the coil. A tantalum shield protected the foil from any potential debris. A copper–rhodium mesh fiducial (100×100-μm mesh spacing with 30-μm-thick wire) was placed halfway between the coil and the proton source. Protons with energy up to 40 MeV were accelerated and detected by a radiochromic film stack placed 8 cm away from the coil.

Experimental Results and Comparison to Synthetic Radiographs

Figure 3 shows experimental radiographs using two different proton energies, taken at 1.1 ns, just after the driving laser has turned off. Overlayed in color are synthetic radiographs, which used a combination of electric charge and current distributions to best recreate the experimental image. The double-plate configuration [Figs. 3(a) and 3(b)] with 0.5-mm spacing shows limited twisting distortion of the mesh. Distortions take two primary forms: a general "pull" on the mesh toward the driven plate to the right on the radiograph and radial "spray" emanating from the wire in all directions in the loop. The general pull is most noticeable when comparing the size of mesh grids on the right and the left of each radiograph, where grids on the right are shrunk and focused compared with those on the left. This is consistent with a large electric field that surrounds all target surfaces and increases with proximity to the driven plate. The radiographs also indicate multiple populations of electrons ejected from the wire material. To recreate the features in the synthetic radiographs, *no current distribution is required in the system*. The energy present in the electrostatic field used to create the synthetic radiographs over the entire simulation box was 36 J, or a conversion rate of nearly 3% from the full laser energy.

The single-plate case shows a significant departure in terms of distortion type. The sheath becomes significantly detached from the coil and does not conform to the shape of the wire. An asymmetric distortion can be seen near the parallel wires, where mesh on top of the loop is expanded and mesh on the bottom is squeezed. This indicates that a current is present that would preferentially flow along the sheath on the inside of the loop since the sheath plasma is a good conductor and the shortest path contains the least inductance for the system. Another indication that a significant current is present in the single-plate case is the twisting of the reference mesh near the parallel wires. A simple rotation of the mesh, as was anticipated in Fig. 1, is not obvious, indicating that a significant electrostatic charge is present in the single-plate case as well. The current used in generating the synthetic radiographs is initially 170 kA at the driven wire and decays as it traverses the loop. The total energy in the magnetic field is approximately 37 J, or a conversion efficiency from the laser of 3.0%. The total energy in the electrostatic field for the

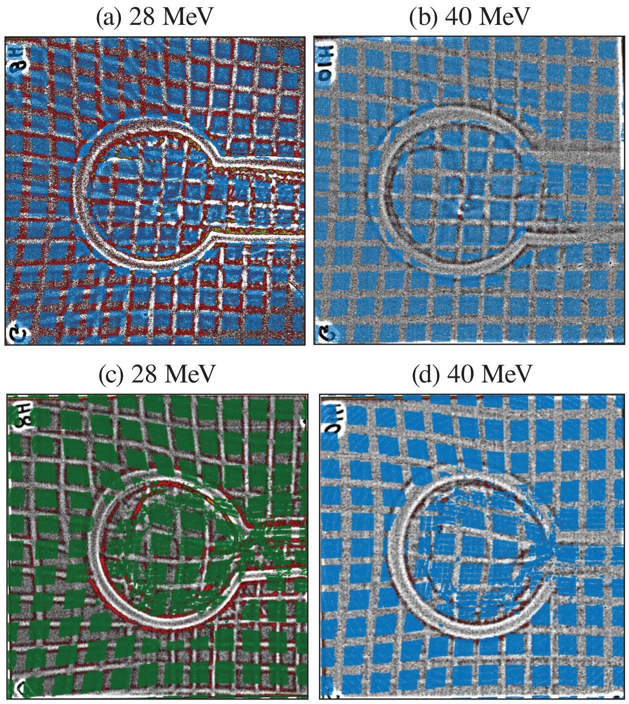

E28999JR

Figure 3
[(a),(b)] Synthetic radiographs created by passing 28- and 40-MeV protons through the fields generated by an electric charge distribution for double-plate experiments. The resulting synthetic radiographs are overlayed on top of the experimental data for comparison. [(c),(d)] A similar treatment for single-plate experiments. A current distribution was required in addition to the charge distribution to reproduce the experimental data in the synthetic radiographs.

simulation box is 20 J, or 1.6% of the incident laser energy. The field is approximately 65 T in the center of the loop; if the current were even throughout the loop, the field would have been much higher at around 140 T.

The proton radiographs from the single-plate experiment indicate that while a current is present, it is in a transient regime for our target design. Angular filter refractometry data and 2-D radiation-hydrodynamic simulations show that radiation ejects electrons from the loop before the current can propagate from the laser-heated region through the connecting solid wire. Therefore, photoelectrons will provide the return current, which allows faster propagation of current than is possible in the unheated copper, consistent with the proton-probing data. Indeed, photoelectrons would be expected to carry the majority of the current since they offer the lowest resistance and lowest inductance path for the current. For our parameters, current propagation in 1.1 ns is observed to be limited to around 3 mm, which is part way around the loop. For most of the other published designs, this would be far enough to drive a current around the entire loop but not far enough to draw any significant current from a second plate. Although current may be present around the entire loop in smaller coils, it could still be nonuniform.

These findings indicate the need to reduce the size of the loop and length of the wire to be as small as possible for LDC's. Doing so creates problems, however, in regard to fielding LDC's in order to magnetize experiments. Reducing the parallel wire length would result in the loop being placed even closer to the driving plate interaction, which would cause more x-ray interference in both the loop and the experiment being magnetized. Placing a shield between the driven plate and magnetized experiment would also prove to be problematic since any x rays will expand material off the shield and cause current to bypass the loop entirely, through the plasma off the shield surface. Reducing the gap between the parallel wires poses a similar problem to the parallel disks, where plasma expansion may simply cause a short circuit. Reducing the loop size removes much of the magnetizing capability of LDC's since loop size determines the size of the system being magnetized. For example, any magnetized inertial fusion concept would require a loop *larger*, not smaller, than the one fielded in our experiments in order to magnetize targets that are typically 1 mm or larger in size.

The data show more potential difficulties for the double-plate–type LDC in addition to those seen with the single plate. First, the driving interaction for the LDC bathes the entire target in x rays, causing significant plasma to form over the entire surface of the LDC. This may be initially beneficial since it will allow current to be drawn more readily, rather than from a cold, solid material. However, the undriven plate is expanded significantly by these x rays due to its proximity to the interaction. The coil is therefore short circuited very quickly before any meaningful magnetic field is generated. This means that the second plate places an upper limitation on energy and intensity of the driving laser, which depends on the spacing between the plates and material. As plate spacing is increased, the coil's inductance is increased to account for the larger gap. It becomes apparent that increasing the plate spacing to address these issues sufficiently will result in a system that tends toward a single-plate design anyway. Adding the additional plate provides benefit only if electrons can be captured by the second plate and the LDC size is small enough that the charge can meaningfully contribute to the current traveling through the loop. Creating an LDC small enough to benefit from the second plate, however, introduces all of the risks of a small LDC system: short circuiting, x-ray interference, and small magnetized volume.

These findings indicate some design considerations for consistent laser-driven coils. First, a single-plate design should be used with minimal distance between the driving plate and coil; in our experiments current appears to propagate significantly for only 3 mm of coil length. The double-plate design appears to offer little benefit for substantial risk and target complexity. Corners should be removed from the loop; even though, in theory, this would result in a less symmetric field, the corners are prime positions for electric-field enhancement, electron emission, and abnormal sheath formation. The laser driver's pulse length should be increased and intensity decreased in order to provide time for the system to respond.

This material is based upon work supported by U.S. Deparment of Energy (DOE) grant DE-SC0016258 from the Office of Fusion Energy Sciences and by the DOE National Nuclear Security Administration under Award Number DE-NA0003856, the University of Rochester, and the New York State Energy Research and Development Authority.

1. G. Fiksel *et al.*, Phys. Rev. Lett. **113**, 105003 (2014).
2. W. Fox, A. Bhattacharjee, and K. Germaschewski, Phys. Rev. Lett. **106**, 215003 (2011).
3. S. A. Slutz *et al.*, Phys. Plasmas **17**, 056303 (2010).
4. D. H. Barnak *et al.*, Phys. Plasmas **24**, 056310 (2017).
5. J. R. Davies *et al.*, Phys. Plasmas **24**, 062701 (2017).
6. H. Nagatomo *et al.*, Nucl. Fusion **53**, 063018 (2013).
7. H. Cai, S. Zhu, and X. T. He, Phys. Plasmas **20**, 072701 (2013).
8. A. Arefiev, T. Toncian, and G. Fiksel, New J. Phys. **18**, 105011 (2016).
9. T. Johzaki *et al.*, Plasma Phys. Control. Fusion **59**, 014045 (2016).
10. G. Gregori *et al.*, Nature **481**, 480 (2012).
11. J. Meinecke *et al.*, Nat. Phys. **10**, 520 (2014).
12. N. C. Woolsey *et al.*, Phys. Plasmas **8**, 2439 (2001).
13. D. B. Schaeffer *et al.*, Phys. Plasmas **19**, 070702 (2012).
14. D. B. Schaeffer *et al.*, Phys. Plasmas **24**, 041405 (2017).

15. H. Daido *et al*., Phys. Rev. Lett. **56**, 846 (1986).

16. J. J. Santos *et al*., New J. Phys. **17**, 083051 (2015).

17. S. Fujioka *et al*., Sci. Rep. **3**, 1170 (2013).

18. K. F. F. Law *et al*., Appl. Phys. Lett. **108**, 091104 (2016).

19. C. Courtois *et al*., J. Appl. Phys. **98**, 054913 (2005).

20. A. Tarifeño, C. Pavez, and L. Soto, J. Phys.: Conf. Ser. **134**, 012048 (2008).

21. L. Gao *et al*., Phys. Plasmas **23**, 043106 (2016).

22. C. Goyon *et al*., Phys. Rev. E **95**, 033208 (2017).

23. W. W. Wang *et al*., Plasma Physics Archive, available at https://arxiv.org/abs/1411.5933v1 (2017).

24. B. J. Zhu *et al*., Appl. Phys. Lett. **107**, 261903 (2015).

25. K. Matsuo *et al*., Phys. Rev. E **95**, 053204 (2017).

26. V. V. Korobkin and S. L. Motylev, Sov. Tech. Phys. Lett. **5**, 474 (1979).

27. V. Ivanov *et al*., Bull. Am. Phys. Soc. **64**, CO8.00008 (2019).

28. G. Fiksel *et al*., Rev. Sci. Instrum. **86**, 016105 (2015).

29. B. B. Pollock *et al*., Rev. Sci. Instrum. **77**, 114703 (2006).

Different Mechanisms of Phase Transformation for Boron in Equilibrium and Under Shock Indicated by Equation-of-State Comparisons

S. Zhang,[1] H. D. Whitley,[2] and T. Ogitsu[2]

[1]Laboratory for Laser Energetics, University of Rochester
[2]Lawrence Livermore National Laboratory

Boron is a prototype for low-Z and superhard materials and a candidate for making ablators for high-energy-density and inertial confinement fusion experiments. Clarifying the structure, stability relation, and melting of the various boron polymorphs at high pressure has long been a subject of interest in materials sciences. Density functional theory (DFT) calculations and diamond-anvil cell (DAC) experiments[1–3] were performed at pressures up to ~200 GPa. Based on these, equilibrium phase diagrams of boron were constructed, which showed high melting temperatures (>4500 K) and a nonicosahedral, metallic α-Ga phase at above 80 to 90 GPa. Dynamic compression experiments were conducted on boron up to 5608 GPa, which measured the pressure–density equation of state (EOS),[4,5] diffraction and electrical conductivity,[6,7] or liquid structure factor[8] along the shock Hugoniot.

In this work, we use first-principles molecular dynamics (MD) to calculate the EOS and shock Hugoniot of various boron phases (α-B_{12}, β, γ-B_{28}, α-Ga, and liquid using different cell shapes), following similar procedures as in Ref. 5. We use a 2000-eV plane-wave basis cutoff, Γ point for Brillouin zone sampling, and simulation cells with 96 to 144 atoms, and generate canonical (NVT) ensembles that consist of 5000 to 10,000 snapshots in each MD simulation.

Our results show that if phase transitions occur in shock-compressed boron at the same pressure–temperature conditions as those expected based on the equilibrium phase diagram, the Hugoniot would have two major discontinuities at 15 and 80 GPa, respectively (Fig. 1). Moreover, melting along the Hugoniot occurs at 1500 to 3500 K and 150 to 250 GPa unless some unknown structure stabilizes over α-Ga at 100 GPa and 2000 K. Discontinuities in Hugoniot density are also expected but are clearly not observed according to the experimental data. Instead, the experimental data appear smooth and follow the trend of our predicted Hugoniot for the α-B_{12} and β-B_{106} phases at up to 80 GPa and follow that of α-B_{12} as well as γ-B_{28} and probably also β-B_{106}, but definitely not α-Ga, at 80 to 112 GPa. These indicate that, instead of transforming into the γ-B_{28} phase, boron under shock compression may remain in the same β or α-B_{12} phase as its initial state up to at least 80 GPa.

In addition, our simulations show that γ-B_{28} melts when temperature increases from 1400 to 1500 K. Therefore, the transformation to γ-B_{28}, if occurring above 80 GPa, would be associated with a jump in temperature and immediately followed by melting or transformation into some other solid structures. Moreover, our DFT-MD simulations show that β-B_{106} remains stable at ~115 GPa and 600 K, and large atomistic displacement or structural instability occurs when temperature exceeds 800 to 1000 K or pressure exceeds 130 GPa. We also find that α-B_{12} remains stable at ~133 GPa and instability occurs at above 150 GPa, for 1000 K or lower temperatures. These data set the upper bounds for β-B_{106} or α-B_{12} samples to remain stable when boron is shocked to above 80 GPa. With stronger shocks above 200 GPa and 3500 K, liquid boron is obtained. Temperatures along the shock Hugoniot are increasingly higher than cold compression along an ambient-temperature isotherm. The transformation kinetics is therefore expected to be slower in room-temperature, static-compression experiments.

Our findings on the phase transitions in shocked boron based on the EOS point of view are supported remarkably well by DAC[9] and explosive-shock[7] experiments with diffraction, which found that β-boron was the stable structure up to ~100 GPa, at which amorphization occurred. It is interesting to note that the Hugoniot temperature of β-B_{106} at 90 GPa is ~600 K according

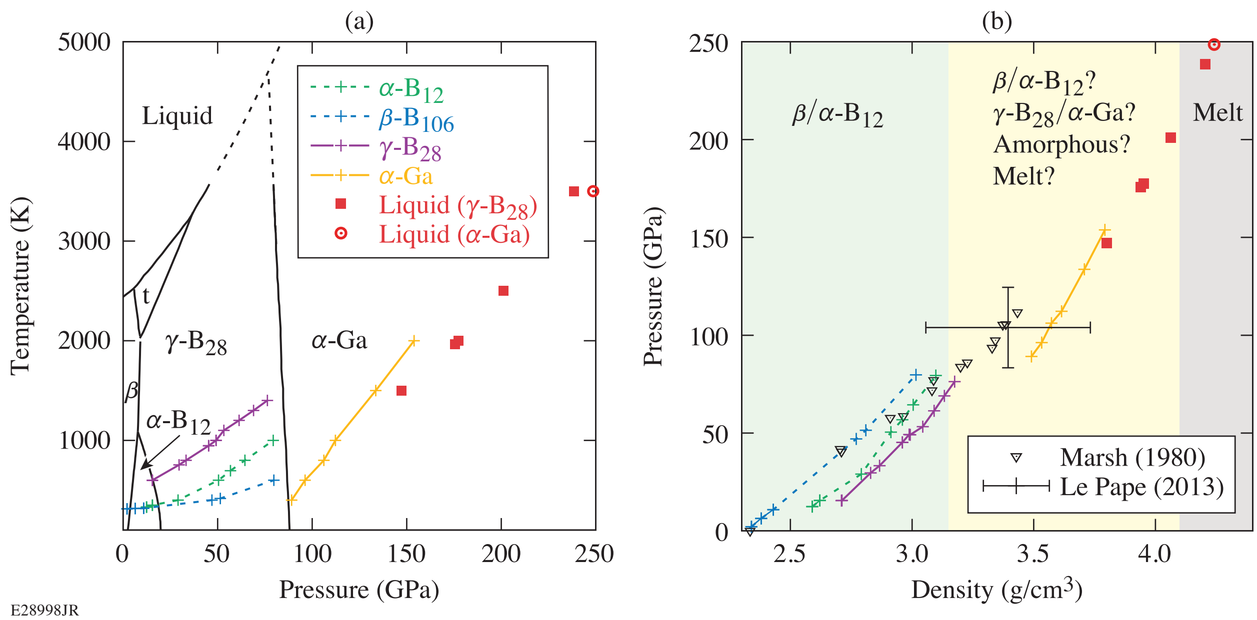

Figure 1
Our first-principles Hugoniots of various boron phases plotted in (a) an equilibrium phase diagram[1,2] and (b) a pressure–density plot in comparison with experimental data.[4,8] The dashed colored curves are expected Hugoniot profiles of β and α-B$_{12}$ phases if the sample is shocked to the corresponding pressures but does not transform to other phases. The lines are guides to the eyes. We approximately divide the Hugoniot into three sections: structure at below ~90 GPa is likely α-B$_{12}$ or β, above ~200 GPa is melt, and between 90 and 200 GPa is uncertain.

to our calculations. The absence of γ-B$_{28}$ or α-Ga phases in the shock experiments, together with findings in laser-heated DAC experiments[10] that heating to ~2000 K is required to make γ-B$_{28}$ or α-Ga phases out of β boron, suggests an energy barrier of 0.05 to 0.17 eV between β and γ/α-Ga phases. The observed amorphization in experiments[7,9] is likely a joint product of the energy barrier that slows down the process of phase transformation and the decreased stability of β boron at megabar pressures.

Our results strongly indicate differences in the mechanisms of phase transitions in equilibrium and under shock and raise questions about kinetics or nonequilibrium processes that materials may undergo during the time scale of the pressure loading.

This material is based upon work supported by the Department of Energy National Nuclear Security Administration under Award Number DE-NA0003856, the University of Rochester, and the New York State Energy Research and Development Authority.

1. A. R. Oganov *et al.*, Nature **457**, 863 (2009); **460**, 292(E) (2009).
2. V. L. Solozhenko and O. O. Kurakevych, Sci. Rep. **3**, 2351 (2013).
3. G. Parakhonskiy *et al.*, Sci. Rep. **1**, 96 (2011).
4. S. P. Marsh, ed. *LASL Shock Hugoniot Data*, Los Alamos Series on Dynamic Material Properties (University of California, Berkeley, CA, 1980).
5. S. Zhang *et al.*, Phys. Rev. **98**, 023205 (2018).

6. A. M. Molodets *et al*., Phys. Solid State **59**, 1406 (2017).

7. A. M. Molodets and A. A. Golyshev, JETP Lett. **108**, 409 (2018).

8. S. Le Pape *et al*., New J. Phys. **15**, 085011 (2013).

9. D. N. Sanz, P. Loubeyre, and M. Mezouar, Phys. Rev. Lett. **89**, 245501 (2002).

10. I. Chuvashova *et al*., Phys. Rev. B **95**, 180102(R) (2017).

A Suite of Neutron Time-of-Flight Detectors to Measure Hot-Spot Motion in Direct-Drive Inertial Confinement Fusion Experiments on OMEGA

O. M. Mannion, J. P. Knauer, V. Yu. Glebov, C. J. Forrest, A. Liu, Z. L. Mohamed, M. H. Romanofsky, T. C. Sangster, C. Stoeckl, and S. P. Regan

Laboratory for Laser Energetics, University of Rochester

In direct-drive inertial confinement fusion (ICF) experiments, a capsule filled with a deuterium–tritium (DT) gas surrounded by a cryogenic DT fuel layer is illuminated by high-power lasers designed to symmetrically compress the target to generate a hot fusing plasma. In experiments where 3-D perturbations exist due to sources such as laser beam pointing errors, laser beam power imbalance, target nonuniformities, or target offsets, the capsule will be compressed asymmetrically. Asymmetric compression of ICF targets reduces the implosion performance by generating residual kinetic energy (RKE) in the target that could have otherwise been used to generate a hotter and denser plasma.[1] Signatures of RKE include a complex flow structure within the fusing hot spot and an asymmetric dense fuel layer. Measuring these signatures of RKE can provide insights into the sources of asymmetries and strategies to improve implosion performance.

Neutron spectroscopy is a particularly useful tool for diagnosing asymmetric compression of ICF targets because neutrons are generated within the fusing plasma and scatter while exiting through the dense fuel layer. This results in the primary unscattered neutron energy spectrum containing information on the state of the fusing hot spot from which they were generated, while the scattered neutron spectrum contains information about the dense fuel layer. In particular, if a collective motion of the hot spot is present in an ICF hot spot, the primary neutron energy spectrum will be Doppler shifted by the hot-spot velocity and will affect measurements the neutron energy spectrum made along various lines of sight differently.[2]

If the neutron velocity is measured along a direction $\hat{d}$, the neutron velocity measured along that line of sight (LOS) is given by

$$v = \langle v_{\text{iso}} \rangle + \langle \vec{u} \cdot \hat{d} \rangle, \tag{1}$$

where v_{iso} is the isotropic neutron velocity, $\vec{u}$ is the hot-spot velocity, and a bracket indicates a neutron-averaged quantity. The isotropic neutron velocity is the sum of the zero-temperature neutron velocity (51,233 km/s for DT neutrons) and the Gamow velocity shift,[3] which is a function of ion temperature and can be written as $v_{\text{iso}} = v_0 + v_{\text{th}}\,(T_{\text{i}})$. By combining multiple measurements of the neutron velocity along different LOS's, the hot-spot velocity $\vec{u}$ and Gamow velocity shift can be determined directly.

To make this measurement, a suite of six neutron time-of-flight detectors has been built and calibrated to measure the primary DT neutron energy spectrum along multiple quasi-orthogonal LOS's on the OMEGA laser. The six detectors, positioned along five LOS's on OMEGA, are shown in Fig. 1 and use either a single detector or a dual collinear or antipodal configuration. The detectors use different technologies including a scintillator coupled to a photomultiplier tube (PMT) detector, a chemical-vapor–deposition diamond-based detector, or a PMT-based detector. By combining the neutron velocity measurements made by each of these detectors, the neutron-averaged hot-spot velocity present in a cryogenic laser-direct-drive implosion has been measured for the first time on OMEGA.

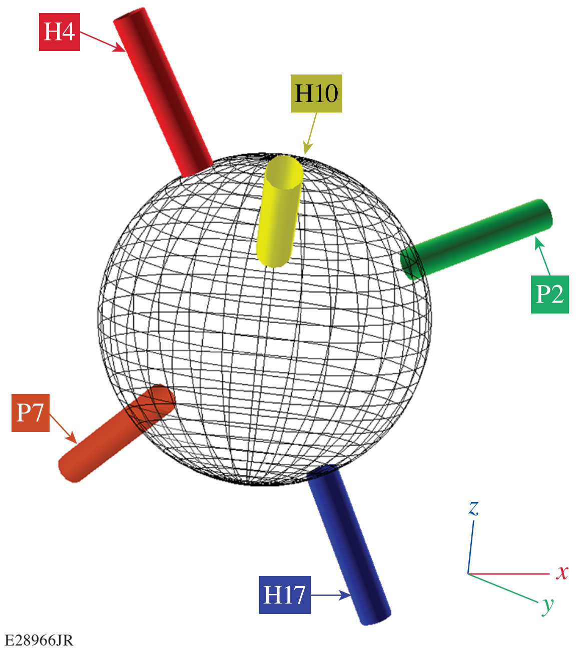

Figure 1
The four axes used on the OMEGA laser for reconstruction of the neutron-averaged hot-spot velocity. The target chamber is represented as a mesh grid, while the five detector LOS's are indicated with cylinders

To validate the velocity measurements made by this detector suite, a set of experiments with large and small target offsets has been studied. Radiation-hydrodynamic simulations predict that if a large target offset is present in direct-drive implosions, a large hot-spot velocity will be observed in the direction of the offset, while zero flow will be observed in the absence of an offset. Measurements of the hot-spot velocity have been made for experiments with both large and small offsets. In experiments with large 52.0-μm and 34.4-μm initial target offsets, large hot-spot velocity magnitudes of 148.9 and 163.7 km/s were measured and the direction was consistent with the initial target offset. In a similar experiment with only a 1.0-μm offset, the hot-spot velocity magnitude was measured to be 60.4 km/s. The presence of a small hot-spot velocity for the zero-offset experiment suggests the presence of a small low-mode asymmetry in either the target or laser system. Despite this, the inferred neutron-averaged hot-spot velocity for targets with large offsets was aligned with the initial target offset directions, consistent with simulation predictions. A summary of these measurements is shown in Fig. 2.

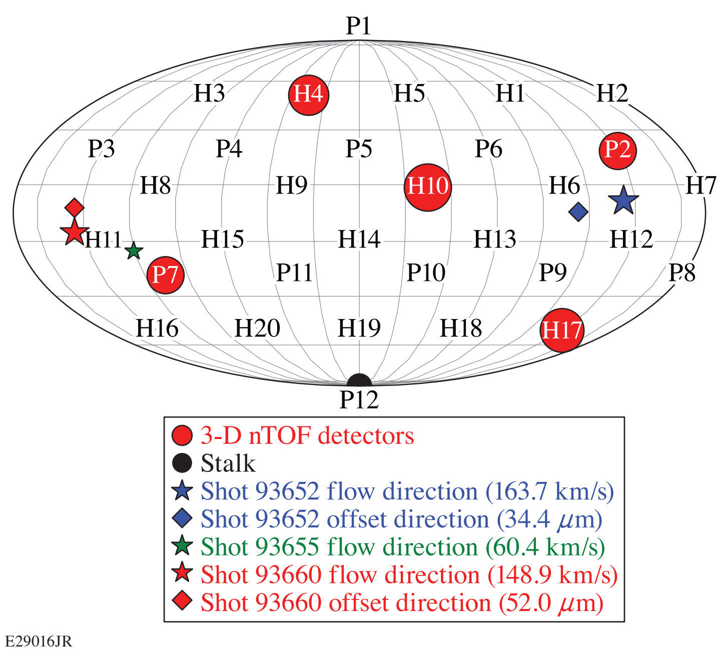

Figure 2
A Mollweide projection of the OMEGA target chamber coordinate system with the neutron-averaged hot-spot velocity reconstruction (stars) inferred from three cryogenic experiments along with their initial target offset direction (diamonds). Two experiments had large target offsets of 34.4 μm with a 52.0-μm offset, while the third had only a 1-μm offset and is not shown. The size of the stars is proportional to the magnitude of the velocity reconstruction. Also shown in red are the ports of LOS's used in the reconstruction.

With the completion of this new diagnostic suite, greater insights into the 3-D behavior of cryogenic experiments will be gained. In particular, the hot-spot velocity measurement will be the primary diagnostic signature of mode-1 asymmetries present in our experiments. These measurements can be used to constrain simulation results and will guide the search for unknown sources of mode-1 asymmetries. Future work will extend this detector suite to include the two measurements of the D–D fusion neutron spectrum that are available on OMEGA.

This material is based upon work supported by the Department of Energy National Nuclear Security Administration under Award Number DE-NA0003856, the University of Rochester, and the New York State Energy Research and Development Authority.

1. B. K. Spears *et al.*, Phys. Plasmas **21**, 042702 (2014).
2. B. Appelbe and J. Chittenden, Plasma Phys. Control. Fusion **53**, 045002 (2011).
3. L. Ballabio, J. Källne, and G. Gorini, Nucl. Fusion **38**, 1723 (1998).

Design of a Free-Space, Image-Relay Optical Time Domain Reflectometer to Measure Fiber-Optic Time Delays at Inertial Confinement Fusion-Relevant Wavelengths

T. Filkins and J. Katz

Laboratory for Laser Energetics, University of Rochester

Fiber optics are used extensively at LLE and other research laboratories to transport critical timing and experimental data. In inertial confinement fusion (ICF) experiments, fibers are used to transport light in the UV, visible, and IR ranges. When a fiber is replaced, a change in the optical path length will introduce a change in the absolute timing of the associated diagnostic. To maintain absolute timing, the change in the fiber-optic time delay (FOTD) must be measured. A commercial optical time domain reflectometer (OTDR) can be used, but only to measure the FOTD at telecom wavelengths, typically in the 800-, 1300-, or 1500-nm range; therefore, it would not provide the relevant FOTD. A simple free-space, image-relay OTDR was designed at LLE that can measure the FOTD at the relevant wavelengths to within 2 ps.

The OTDR requires a short-pulse laser source, simple optics and optomechanics, a photodetector, and a fast oscilloscope. For this setup, the OMEGA 60 2ω fiducial and Diagnostic Support and Development Laboratory (DSDL) 3ω laser pulses were used as the laser source to measure the FOTD of an ~16-m-long, large-core Russian graded-index fiber at two wavelengths relevant to ICF experiments (see Fig. 1). The fiber-launched laser light was collimated with a Thorlabs aspheric fiber-coupled collimator. The light was then coupled into the test fiber using a second collimator. The Fresnel reflections off the input and output surfaces of the test fiber were then transported to a large-core step-index collection fiber with a broadband pellicle beam splitter and coupled with a third collimator. The collection fiber was coupled with a fast (less than 100 ps) photodetector that was coupled to a fast-oscilloscope sampling at 40 GSa/s.

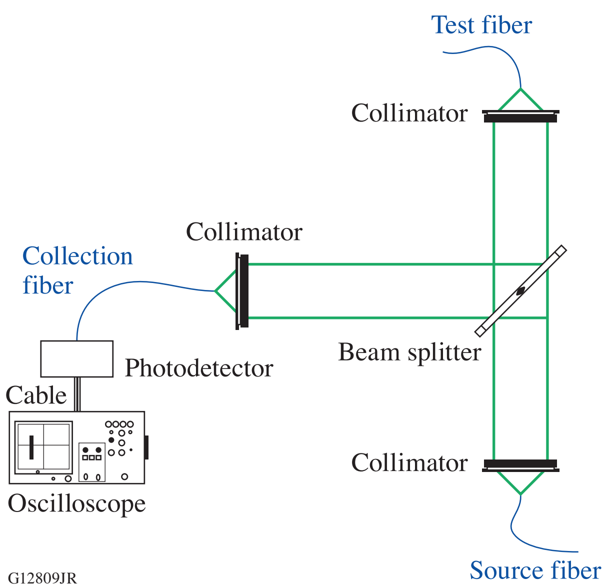

Figure 1
A short-pulse laser with a width of 10 ps from the DSDL or a 2-GHz comb from the OMEGA fiducial is used to measure the FOTD of the test fiber. Two different photodetectors were used to digitize the signals: a Hamamatsu biplanar phototube (R1328U-53) or a Hamamatsu GaAs photodiode (G4176-01). The phototube had better signal-to-noise ratio, which led to smaller uncertainties.

The signals on the oscilloscope (Fig. 2) were fitted with Gaussian functions to determine the centroid of each peak. The distance between corresponding peaks was twice the FOTD. The uncertainty of the fits was found by using methods outlined by Bobroff.[1] With a strong signal-to-noise ratio, and taking advantage of eight simultaneous measurements, the uncertainty of the FOTD was determined to be about 2 ps.

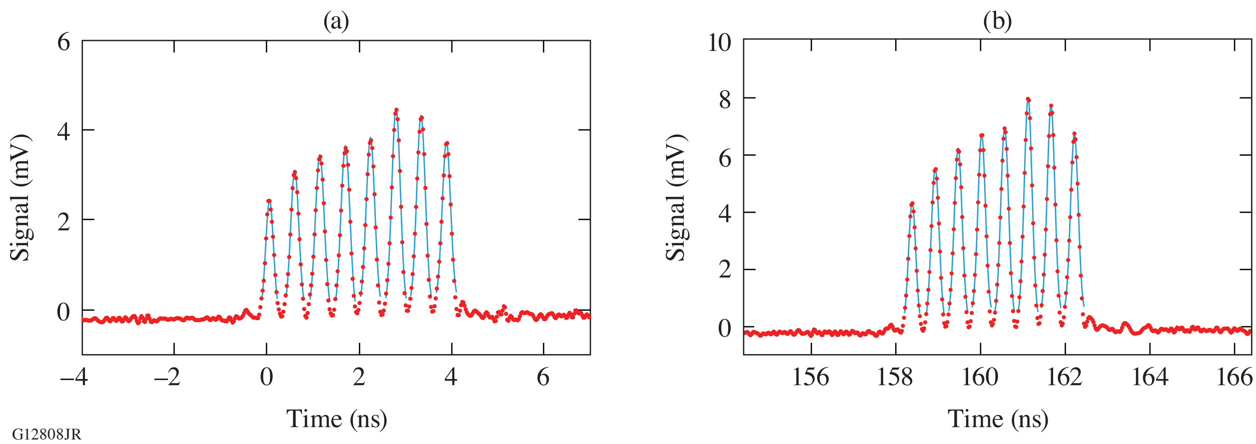

Figure 2
The (a) input surface and (b) output surface reflections were captured on a single trace in one channel and with the same detector, which eliminated any skew that might have been present between channels in the oscilloscope and removed any uncertainty about instrument response variations in the analysis between the two signals.

This material is based upon work supported by the Department of Energy National Nuclear Security Administration under Award Number DE-NA0003856, the University of Rochester, and the New York State Energy Research and Development Authority.

1. N. Bobroff, Rev. Sci. Instrum. **57**, 1152 (1986).

FY20 Q1 Laser Facility Report

J. Puth, M. Labuzeta, D. Canning, and R. T. Janezic

Laboratory for Laser Energetics, University of Rochester

During the first quarter of FY20, the Omega Laser Facility conducted 301 target shots on OMEGA and 242 target shots on OMEGA EP for a total of 543 target shots (see Tables I and II). OMEGA averaged 11.0 target shots per operating day, averaging 93.0% Availability and 94.7% Experimental Effectiveness.

OMEGA EP was operated extensively in the first quarter of FY20 for a variety of user experiments. OMEGA EP averaged 9.7 target shots per operating day averaging 95.2% Availability and 96.5% Experimental Effectiveness.

Table I: OMEGA Laser System target shot summary for Q1 FY20.

Program	Laboratory	Planned Number of Target Shots	Actual Number of Target Shots
ICF	LLE	99	98
	LLNL	5.5	6
ICF Subtotal		104.5	104
HED	LLE	22	21
	LANL	22	25
	LLNL	27.5	31
	SNL	11	9
HED Subtotal		82.5	86
LBS	LLE	11	13
	LLNL	16.5	19
	Princeton University	11	11
LBS Subtotal		38.5	43
NLUF		22	24
LLE Calibration	LLE	0	44
Grand Total		247.5	301

Table II: OMEGA EP Laser System target shot summary for Q1 FY20.

Program	Laboratory	Planned Number of Target Shots	Actual Number of Target Shots
ICF	LLE	28	53
	LLNL	21	31
ICF Subtotal		**49**	**84**
HED	LLE	14	24
	LLNL	21	28
	SNL	7	15
HED Subtotal		**42**	**67**
LBS	LANL	7	1
	LLNL	14	27
LBS Subtotal		**21**	**28**
NLUF		28	31
LaserNetUS		14	23
LLE Calibration	LLE	0	9
Grand Total		**154**	**242**

Accomplishments During Q1 FY20

A novel cryogenic microscope was deployed in the Cryogenic and Tritium Facility to image a cryogenic DT target for submicron features. The key finding was that a filled DT target could be nondestructively imaged at a 0.6-μm resolution. Three 180 $\times$ 280-μm areas were carefully sampled, and new features resulting from the filling operations were counted and analyzed. Based on these three areas, it is estimated that approximately 670 new features appeared from the fill operations. The limb of the target was imaged, and across the entire target, ten new features of 1 to 3 μm in size were discovered on the outside of the shell. The system was unable to determine if the estimated 670 features are predominantly on the outside or inside of the shell. Further work with this new microscope will continue.

The final layer of shielding has been installed between the OMEGA Target Bay and LaCave with measured reduction in the noise level by as much as 50% (depending on location).

Publications and Conference Presentations

Publications

A. Antikainen and G. P. Agrawal, "Supercontinuum Generation in Seven-Core Fibers," J. Opt. Soc. Am. B **36**, 2927 (2019).

P. T. Campbell, D. Canning, A. E. Hussein, K. D. W. Ratnayaka, A. G. R. Thomas, K. Krushelnick, and L. Willingale, "Proton Beam Emittance Growth in Multipicosecond Laser-Solid Interactions," New J. Phys. **21**, 103021 (2019).

A. S. Davies, D. Haberberger, J. Katz, S. Bucht, J. P. Palastro, R. K. Follett, and D. H. Froula, "Investigation of Picosecond Thermodynamics in a Laser-Produced Plasma Using Thomson Scattering," Plasma Phys. Control. Fusion **62**, 014012 (2020).

C. Fagan, M. Sharpe, W. T. Shmayda, and W. U. Schröder, "Tritium Retention in Hexavalent Chromate-Conversion–Coated Aluminum Alloy," Fusion Sci. Technol. **75**, 1058 (2019).

S. R. Fairchild, Y. Liu, J. Palastro, and J. Peñano, "Laser Filamentation and Applications: Introduction," J. Opt. Soc. Am. B **36**, LFA1 (2019).

P. Franke, D. Turnbull, J. Katz, J. P. Palastro, I. A. Begishev, J. Bromage, J. L. Shaw, R. Boni, and D. H. Froula, "Measurement and Control of Large Diameter Ionization Waves of Arbitrary Velocity," Opt. Express **27**, 31978 (2019).

T. Gong, H. Habara, K. Sumioka, M. Yoshimoto, Y. Hayashi, S. Kawazu, T. Otsuki, T. Matsumoto, T. Minami, K. Abe, K. Aizawa, Y. Enmei, Y. Fujita, A. Ikegami, H. Makiyama, K. Okazaki, K. Okida, T. Tsukamoto, Y. Arikawa, S. Fujioka, Y. Iwasa, S. Lee, H. Nagatomo, H. Shiraga, K. Yamanoi, M. S. Wei, and K. A. Tanaka, "Direct Observation of Imploded Core Heating via Fast Electrons with Super-Penetration Scheme," Nat. Commun. **10**, 5614 (2019).

G. Guidarelli, J. Nordhaus, L. Chamandy, Z. Chen, E. G. Blackman, A. Frank, J. Carroll-Nellenback, and B. Liu, "Hydrodynamic Simulations of Disrupted Planetary Accretion Discs Inside the Core of an AGB Star," Mon. Not. R. Astron. Soc. **490**, 1179 (2019).

D. Haberberger, A. Shvydky, V. N. Goncharov, D. Cao, J. Carroll-Nellenback, S. X. Hu, S. T. Ivancic, V. V. Karasiev, J. P. Knauer, A. V. Maximov, and D. H. Froula, "Plasma Density Measurements of the Inner Shell Release," Phys. Rev. Lett. **123**, 235001 (2019).

A. M. Hansen, D. Turnbull, J. Katz, and D. H. Froula, "Mitigation of Self-Focusing in Thomson Scattering Experiments," Phys. Plasmas **26**, 103110 (2019).

M. H. Helle, G. DiComo, S. Gregory, A. Mamonau, D. Kaganovich, R. Fischer, J. Palastro, S. Melis, and J. Peñano, "Beating Optical-Turbulence Limits Using High-Peak-Power Lasers," Phys. Rev. Appl. **12**, 054043 (2019).

S. X. Hu, R. Epstein, W. Theobald, H. Xu, H. Huang, V. N. Goncharov, S. P. Regan, P. W. McKenty, R. Betti, E. M. Campbell, and D. S. Montgomery, "Direct-Drive Double-Shell Implosion: A Platform for Burning-Plasma Physics Studies," Phys. Rev. E **100**, 063204 (2019).

T. Z. Kosc, A. A. Kozlov, S. Papernov, K. R. P. Kafka, K. L. Marshall, and S. G. Demos, "Investigation of Parameters Governing Damage Resistance of Nematic Liquid Crystals for High-Power or Peak-Intensity Laser Applications," Sci. Rep. **9**, 16435 (2019).

J. Levesque, C. Kuranz, T. Handy, M. Manuel, and F. Fiuza, "Characterizing Filamentary Magnetic Structures in Counter-Streaming Plasmas by Fourier Analysis of Proton Images," Phys. Plasmas **26**, 102303 (2019).

J. F. Myatt, J. G. Shaw, R. K. Follett, D. H. Edgell, D. H. Froula, J. P. Palastro, and V. N. Goncharov, "*LPSE*: A 3-D Wave-Based Model of Cross-Beam Energy Transfer in Laser-Irradiated Plasmas," J. Comp. Phys. **399**, 108916 (2019).

J. M. Ngoko Djiokap, A. V. Meremianin, N. L. Manakov, L. B. Madsen, S. X. Hu, and A. F. Starace, "Molecular Symmetry-Mixed Dichroism in Double Photoionization of H_2," Phys. Rev. Lett. **123**, 143202 (2019).

C. E. Parker, J. A. Frenje, O. H. W. Siegmund, C. J. Forrest, V. Yu. Glebov, J. D. Kendrick, C. W. Wink, M. Gatu Johnson, T. J. Hilsabeck, S. T. Ivancic, J. Katz, J. D. Kilkenny, B. Lahmann, C. K. Li, F. H. Séguin, C. M. Sorce, C. Trosseille, and R. D. Petrasso, "Response of a Lead-Free Borosilicate-Glass Microchannel Plate to 14-MeV Neutrons and γ-Rays," Rev. Sci. Instrum. **90**, 103306 (2019).

R. Paul, S. X. Hu, and V. V. Karasiev, "Crystalline Phase Transitions and Vibrational Spectra of Silicon up to Multiterapascal Pressures," Physical Review B **100**, 144101 (2019).

J. J. Ruby, J. R. Rygg, J. A. Gaffney, B. Bachmann, and G. W. Collins, "A Boundary Condition for Guderley's Converging Shock Problem," Phys. Fluids **31**, 126104 (2019).

E. M. Schiesser, S.-W. Bahk, J. Bromage, and J. P. Rolland, "Design and Alignment of an All-Spherical Unobscured Four-Mirror Image Relay for an Ultra-Broadband Sub-Petawatt Laser," Appl. Optics **58**, 9514 (2019).

E. M. Schiesser, A. Bauer, and J. P. Rolland, "Effect of Freeform Surfaces on the Volume and Performance of Unobscured Three Mirror Imagers in Comparison with Off-Axis Rotationally Symmetric Polynomials," Opt. Express **27**, 21,750 (2019).

E. M. Schiesser, A. Bauer, and J. P. Rolland "Estimating Field-Dependent Nodal Aberration Theory Coefficients from Zernike Full-Field Displays by Utilizing Eight-Order Astigmatism," J. Opt. Soc. Am. A **36**, 2115 (2019).

M. Sharpe, C. Fagan, and W. T. Shmayda, "Distribution of Tritium in the Near Surface of Type 316 Stainless Steel," Fusion Sci. Technol. **75**, 1053 (2019).

W. T. Shmayda, C. R. Shmayda, and G. Torres, "Tritium Extraction from Water," Fusion Sci. Technol. **75**, 1030 (2019).

F. Soubiran, F. González-Cataldo, K. P. Driver, S. Zhang, and B. Militzer, "Magnesium Oxide at Extreme Temperatures and Pressures Studied with First-Principles Simulations," J. Chem. Phys. **151**, 214104 (2019).

L. L. Taylor, J. Xu, M. Pomerantz, T. R. Smith, J. C. Lambropoulos, and J. Qiao, "Femtosecond Laser Polishing of Germanium," Opt. Mater. Express **9**, 4165 (2019) (invited).

H. Wen, A. V. Maximov, R. Yan, J. Li, C. Ren, and F. S. Tsung, "Three-Dimensional Particle-in-Cell Modeling of Parametric Instabilities Near the Quarter-Critical Density in Plasmas," Physical Review E **100**, 041201(R) (2019).

K. Werner, V. Gruzdev, N. Talisa, K. Kafka, D. Austin, C. M. Liebig, and E. Chowdhury, "Single-Shot Multi-Stage Damage and Ablation of Silicon by Femtosecond Mid-infrared Laser Pulses," Sci. Rep. **9**, 19993 (2019).

A. B. Zylstra, H. W. Herrmann, Y. H. Kim, A. McEvoy, K. Meaney, V. Yu. Glebov, C. Forrest, and M. Rubery, "Improved Calibration of the OMEGA Gas Cherenkov Detector," Rev. Sci. Instrum. **90**, 123504 (2019)

A. B. Zylstra, H. G. Rinderknecht, J. A. Frenje, C. K. Li, and R. D. Petrasso, "Modified Parameterization of the Li-Petrasso Charged-Particle Stopping Power Theory," Phys. Plasmas **26**, 122703 (2019).

Forthcoming Publications

M. Bailly-Grandvaux, J. Kim, C. M. Krauland, S. Zhang, M. Dozières, M. S. Wei, W. Theobald, P. E. Grabowski, J. J. Santos, Ph. Nicolaï, P. McKenna, M. P. Desjarlais, and F. N. Beg, "Transport of kJ-Laser-Driven Relativistic Electron Beams in Cold and Shock-Heated Vitreous Carbon and Diamond," to be published in the New Journal of Physics.

X. Bian, H. Aluie, D. Zhao, H. Zhang, and D. Livescu, "Revisiting the Late-Time Growth of Single-Mode Rayleigh–Taylor Instability and the Role of Vorticity," to be published in Physica D: Nonlinear Phenomena.

L. E. Chen, A. F. A. Bott, P. Tzeferacos, A. Rigby, A. Bell, R. Bingham, C. Graziani, J. Katz, M. Koenig, C. K. Li, R. Petrasso, H.-S. Park, J. S. Ross, D. Ryu, T. G. White, B. Reville, J. Matthews, J. Meinecke, F. Miniati, E. G. Zweibel, S. Sarkar, A. A. Schekochihin, D. Q. Lamb, D. H. Froula, and G. Gregori, "Transport of High-Energy Charged Particles Through Spatially Intermittent Turbulent Magnetic Fields," to be published in the Astrophysical Journal.

S. Depierreux, C. Neuville, V. Tassin, M.-C. Monteil, P.-E. Masson-Laborde, C. Baccou, P. Fremerye, F. Philippe,

P. Seytor, D. Teychenné, J. Katz, R. Bahr, M. Casanova, N. Borisenko, L. Borisenko, A. Orekhov, A. Colaitis, A. Debayle, G. Duchateau, A. Heron, S. Huller, P. Loiseau, P. Nicolai, C. Riconda, G. Tran, C. Stoeckl, W. Seka, V. Tikhonchuk, D. Pesme, and C. Labaune, "Experimental Investigation of the Collective Stimulated Brillouin and Raman Scattering of Multiple Laser Beams in Inertial Confinement Fusion Experiments," to be published in Plasma Physics and Controlled Fusion.

C. Dorrer, E. M. Hill, and J. D. Zuegel, "High-Energy Parametric Amplification of Spectrally Incoherent Broadband Pulses," to be published in Optics Express.

M. Dozières, S. Hansen, P. Forestier-Colleoni, C. McGuffey, D. Kawahito, M. Bailly-Grandvaux, K. Bhutwala, C. M. Krauland, M. S. Wei, P. Gourdain, J. R. Davies, K. Matsuo, S. Fujioka, E. M. Campbell, J. L. Peebles, J. J. Santos, D. Batani, S. Zhang, and F. N. Beg, "Characterization of an Imploding Cylindrical Plasma for Electron Transport Studies Using X-Ray Emission Spectroscopy," to be published in Physics of Plasmas.

C. Fagan, M. Sharpe, W. T. Shmayda, and W. U. Schröder, "Thin-Alumina Film as a Tritium Adsorption Inhibitor for Stainless-Steel 316," to be published in Fusion Science and Technology.

M. Gatu Johnson, P. J. Adrian, K. S. Anderson, B. D. Appelbe, J. P. Chittenden, A. J. Crilly, D. Edgell, C. J. Forrest, J. A. Frenje, V. Yu. Glebov, B. M. Haines, I. Igumenshchev, D. Jacobs-Perkins, R. Janezic, N. V. Kabadi, J. P. Knauer, B. Lahmann, O. M. Mannion, F. J. Marshall, T. Michel, F. H. Séguin, R. Shah, C. Stoeckl, C. A. Walsh, and R. D. Petrasso, "Impact of Stalk on Directly Driven Inertial Confinement Fusion Implosions," to be published in Physics of Plasmas.

M. J. Guardalben, M. Barczys, B. E. Kruschwitz, M. Spilatro, L. J. Waxer, and E. M. Hill, "Laser System Model for Enhanced Operational Performance and Flexibility on OMEGA EP," to be published in High Power Laser Science and Engineering.

B. M. Haines, R. C. Shah, J. M. Smidt, B. J. Albright, T. Cardenas, M. R. Douglas, C. Forrest, V. Yu. Glebov, M. A. Gunderson, C. E. Hamilton, K. C. Henderson, Y. Kim, M. N. Lee, T. J. Murphy, J. A. Oertel, R. E. Olson, B. M. Patterson, R. B. Randolph, and D. W. Schmidt, "Observation of Persistent Species Temperature Separation in Inertial Confinement Fusion Mixtures," to be published in Nature Communications.

V. V. Ivanov, A. V. Maximov, A. L. Astanovitskiy, I. A. Begishev, R. Betti, J. R. Davies, C. Mileham, J. D. Moody, C. Stoeckl, K. J. Swanson, N. L. Wong, and J. Bromage, "Study of Laser-Driven Magnetic Fields with a Continuous Wave Faraday Rotation Diagnostic," to be published in Physics of Plasmas.

T. Z. Kosc, H. Huang, T. J. Kessler, A. Maltsev, and S. G. Demos, "Measurement of the Angular Dependence of the Spontaneous Raman Scattering in Anisotropic Crystalline Materials Using Spherical Samples: Potassium Dihydrogen Phosphate as a Case Example," to be published in Review of Scientific Instruments.

L. S. Leal, A. V. Maximov, R. Betti, A. B. Sefkow, and V. V. Ivanov, "Modeling Magnetic Confinement of Laser-Generated Plasma in Cylindrical Geometry Leading to Disk-Shaped Structures," to be published in Physics of Plasmas.

K. Luo, V. V. Karasiev, and S. B. Trickey, "Towards Accurate Orbital-Free Simulations: A Generalized Gradient Approximation for the Noninteracting Free Energy Density Functional," to be published in Physical Review B.

S. MacNally, C. Smith, J. Spaulding, J. Foster, and J. B. Oliver, "Glancing-Angle–Deposited Silica Films for Ultraviolet Wave Plates," to be published in Applied Optics.

O. M. Mannion, J. P. Knauer, V. Yu. Glebov, C. J. Forrest, A. Liu, Z. L. Mohamed, M. H. Romanofsky, T. C. Sangster, C. Stoeckl, and S. P. Regan, "A Suite of Neutron Time-of-Flight Detectors to Measure Hot-Spot Motion in Direct-Drive Inertial Confinement Fusion Experiments on OMEGA," to be published in Nuclear Instruments and Methods in Physics Research A: Accelerators, Spectrometers, Detectors, and Associated Equipment.

A. L. Milder, H. Le, M. Sherlock, P. Franke, J. Katz, S. T. Ivancic, J. L. Shaw, J. P. Palastro, A. M. Hansen, I. A. Begishev, W. Rozmus, and D. H. Froula, "Evolution of the Electron Distribution Function in the Presence of Inverse Bremsstrahlung Heating and Collisional Ionization," to be published in Physical Review Letters.

M. Millot, S. Zhang, D. E. Fratanduono, F. Coppari, S. Hamel, B. Militzer, D. Simonova, S. Shcheka, N. Dubrovinskaia, L. Dubrovinksy, and J. H. Eggert, "Recreating Giant Impacts in the Laboratory: Shock Compression of $MgSiO_3$ Bridgmanite to 14 Mbar," to be published in Geophysical Research Letters.

J. Nilsen, A. L. Kritcher, M. E. Martin, R. E. Tipton, H. D. Whitley, D. C. Swift, T. Döppner, B. L. Bachmann, A. E.

Lazicki, N. B. Kostinski, B. R. Maddox, G. W. Collins, S. H. Glenzer, and R. W. Falcone, "Understanding the Effects of Radiative Preheat and Self-Emission from Shock Heating on Equation of State Measurement at 100s of Mbar Using Spherically Converging Shock Waves in a NIF Hohlraum," to be published in Matter and Radiation at Extremes.

J. B. Oliver, A. L. Rigatti, T. Noll, J. Spaulding, J. Hettrick, V. Gruschow, G. Mitchell, D. Sadowski, C. Smith, and B. Charles, "Large-Aperture Coatings for Fusion-Class Laser Systems," to be published in Applied Optics.

J. B. Oliver, J. Spaulding, and B. Charles, "Stress Compensation by Deposition of a Nonuniform Corrective Coating," to be published in Applied Optics.

J. P. Palastro, J. L. Shaw, P. Franke, D. Ramsey, T. T. Simpson, and D. H. Froula, "Dephasingless Laser Wakefield Acceleration," to be published in Physical Review Letters.

V. A. Smalyuk, C. R. Weber, O. L. Landen, S. Ali, B. Bachmann, P. M. Celliers, E. L. Dewald, A. Fernandez, B. A. Hammel, G. Hall, A. G. MacPhee, L. Pickworth, H. F. Robey, N. Alfonso, K. L. Baker, L. F. Berzak Hopkins, L. Carlson, D. T. Casey, D. S. Clark, J. Crippen, L. Divol, T. Döppner, M. J. Edwards, M. Farrell, S. Felker, J. E. Field, S. W. Haan, A. V. Hamza, M. Havre, M. C. Herrmann, W. W. Hsing, S. Khan, J. Kline, J. J. Kroll, S. LePape, E. Loomis, B. J. MacGowan, D. Martinez, L. Masse, M. Mauldin, J. L. Milovich, A. S. Moore, A. Nikroo, A. Pak, P. K. Patel, J. L. Peterson, K. Raman, B. A. Remington, N. Rice, M. Schoff, and M. Stadermann, "Review of Hydrodynamic Instability Experiments in Inertially Confined Fusion Implosions on the National Ignition Facility," to be published in Plasma Physics and Controlled Fusion.

C. Smith, S. MacNally, and J. B. Oliver, "Ellipsometric Modeling of Serially Bi-Deposited Glancing-Angle–Deposition Coatings," to be published in Applied Optics.

R. Sobolewski, "Optical Detectors and Sensors," to be published in the Handbook of Superconducting Materials.

W. Theobald, C. Sorce, W. R. Donaldson, R. Epstein, R. L. Keck, C. Kellogg, T. J. Kessler, J. Kwiatkowski, F. J. Marshall, S. Sampat, W. Seka, R. C. Shah, A. Shvydky, C. Stoeckl, L. J. Waxer, and S. P. Regan, "Inferred UV Fluence Focal-Spot Profiles from Soft X-Ray Pinhole-Camera Measurements on OMEGA," to be published in Review of Scientific Instruments.

D. Turnbull, A. Colaïtis, A. M. Hansen, A. L. Milder, J. P. Palastro, J. Katz, C. Dorrer, B. E. Kruschwitz, D. J. Strozzi, and D. H. Froula, "Impact of the Langdon Effect on Cross-Beam Energy Transfer," to be published in Nature Physics.

J. Zhang, R. Wei, M. Elkabbash, E. M. Campbell, and C. Guo, "Thin-Film Perfect Infrared Absorbers over Single- and Dual-Band Atmospheric Windows," to be published in Optics Letters.

S. Zhang, C. M. Krauland, J. Peebles, J. Li, F. N. Beg, N. Alexander, W. Theobald, R. Betti, D. Haberberger, E. M. Campbell, R. Yan, E. Borwick, C. Ren, and M. S. Wei, "Experimental Study of Hot-Electron Generation in Shock-Ignition Relevant High-Intensity Regime with Large-Scale Hot Plasmas," to be published in Physics of Plasmas.

Y. Zhao and W. R. Donaldson, "Ultrafast UV AlGaN Metal–Semiconductor–Metal Photodetector with a Response Time Below 25 ps," to be published in the IEEE Journal of Quantum Electronics.

A. B. Zylstra, J. R. Rygg, G. W. Collins, C. K. Li, J. A. Frenje, R. D. Petrasso, S. R. Nagel, P. Fitzsimmons, and H. Reynolds, Platform Development for dE/dx Measurements on Short-Pulse Laser Facilities," to be published in High Energy Density Physics.

Conference Presentations

W. Theobald, "Review of the LLE-CELIA Shock-Ignition Collaboration over the Last Ten Years," presented at the CELIA Anniversary, Talence, France, 1 October 2019.

C. Dorrer and S.-W. Bahk, "Characterization of Spatiotemporal Coupling with Multispectral Hartmann Wavefront Sensor," presented at Ultrafast Optics XII, Bol, Croatia, 6–11 October 2019.

M. S. Wei, J. D. Zuegel, H. G. Rinderknecht, J. Bromage, P. M. Nilson, S. X. Hu, D. H. Froula, F. Albert, B. M. Hegelich, M. Roth, and E. M. Campbell, "EP OPAL: A Multibeam Ultrahigh-Intensity Laser User Facility for New Frontiers in High-Energy-Density and Relativistic Physics," presented at the First ELI-NP User Workshop, Magurele, Romania, 7–11 October 2019.

M. S. Wei, "LaserNetUS," presented at the Laserlab Conference, Florence, Italy, 11 October 2019.

C. J. Forrest, V. Yu. Glebov, J. P. Knauer, O. M. Mannion, Z. Mohamed, P. B. Radha, S. P. Regan, T. C. Sangster, A. Schwemmlein, C. Stoeckl, W. U. Schröder, and G. M. Hale, "Inelastic Reaction of 14-MeV Neutrons with ^{7}Li," presented at the APS Division of Nuclear Physics Fall Meeting, Arlington, VA, 14–17 October 2019.

The following presentations were made at the 61st Meeting of the American Physical Society Division of Plasma Physics, Fort Lauderdale, FL, 21–25 October 2019:

K. S. Anderson, J. A. Marozas, D. Cao, C. J. Forrest, O. M. Mannion, R. C. Shah, P. B. Radha, F. J. Marshall, T. J. B. Collins, J. P. Knauer, V. N. Goncharov, and M. Gatu Johnson, "Cross-Beam Energy Transfer in Offset Implosions on OMEGA."

Z. Barfield, D. H. Froula, and J. L. Peebles, "The Study of Thermal Transport in Magnetized Laser-Produced Plasmas."

D. Barnak, K. Flippo, C. Kawaguchi, K. Kelso, H. Li, S. Li, E. Loomis, Y. Lu, N. Vazirani, A. Birkel, B. Lahmann, and C. K. Li, "Impact of Self-Generated B-Fields on High-Energy-Density Experiments."

G. Bruhaug, H. G. Rinderknecht, M. S. Wei, G. W. Collins, J. R. Rygg, and J. L. Shaw, "An Investigation of Monoenergetic Electron Beams for High-Energy-Density and Inertial Confinement Fusion Diagnostics."

D. Cao, D. Patel, M. J. Rosenberg, W. Theobald, C. Stoeckl, A. R. Christopherson, I. V. Igumenshchev, V. Gopalaswamy, S. P. Regan, C. Thomas, P. B. Radha, R. Betti, and V. N. Goncharov, "Implosion Designs Varying Hot-Electron Production for Direct-Drive Inertial Confinement Fusion Implosions on OMEGA."

A. R. Christopherson, R. Betti, W. Theobald, C. J. Forrest, M. Wei, E. M. Campbell, J. Howard, M. J. Rosenberg, A. A. Solodov, D. Patel, J. A. Delettrez, C. Stoeckl, D. Edgell, W. Seka, V. Yu. Glebov, A. K. Davis, J. L. Peebles, A. V. Maximov, R. Simpson, M. Gatu Johnson, W. Scullin, V. Gopalaswamy, D. Cao, V. N. Goncharov, P. B. Radha, S. P. Regan, and R. Epstein, "Direct Measurements of Hot-Electron Preheat in the Dense Fuel of Inertial Confinement Fusion Implosions" (invited).

T. J. B. Collins, C. Stoeckl, R. Epstein, S. Miller, J. A. Marozas, K. S. Anderson, D. Cao, O. M. Mannion, R. Betti, J. A. Delettrez, W. A. Bittle, C. J. Forrest, V. Yu. Glebov, V. N. Goncharov, D. R. Harding, I. V. Igumenshchev, D. W. Jacobs-Perkins, R. T. Janezic, J. H. Kelly, T. Z. Kosc, C. Mileham, D. T. Michel, R. L. McCrory, P. W. McKenty, F. J. Marshall, S. F. B. Morse, P. B. Radha, S. P. Regan, B. Rice, T. C. Sangster, M. J. Shoup III, W. T. Shmayda, C. Sorce, W. Theobald, J. Ulreich, M. D. Wittman, J. A. Frenje, M. Gatu Johnson, and R. D. Petrasso, "Mixing at the Fuel–Ablator Interface in Backlit OMEGA Cryogenic Implosions."

R. S. Craxton, A. Sharma, Y. Yang, R. F. Heeter, Y. P. Opachich, T. Cardenas, H. M. Johns, and T. S. Perry, "Simulations of Double Cone-in-Shell Implosions for an X-Ray Backlighting Source at the National Ignition Facility."

J. R. Davies, D. H. Barnak, R. Betti, T. Cracium, and J. L. Peebles, "Current Transients in Laser-Driven Coils."

D. H. Edgell, R. E. Bahr, J. Katz, and D. H. Froula, "Absorption and Scattered-Light Asymmetry in OMEGA Implosions."

R. Epstein, C. Stoeckl, P. B. Radha, T. J. B. Collins, D. Cao, R. C. Shah, D. Cliche, and R. C. Mancini, "Self-Radiography of Imploded Shells on OMEGA Based on Additive-Free Multi-Monochromatic Continuum Spectral Analysis."

R. K. Follett, J. G. Shaw, D. H. Edgell, D. H. Froula, C. Dorrer, J. Bromage, E. M. Hill, T. J. Kessler, A. V. Maximov, A. A. Solodov, E. M. Campbell, J. P. Palastro, J. F. Myatt, J. W. Bates, and J. L. Weaver, "Broadband Mitigation of Laser–Plasma Instabilities."

P. Franke, J. P. Palastro, D. Turnbull, and D. H. Froula, "Frequency Conversion of Laser Pulses Reflected from Ionization Waves of Arbitrary Velocity."

D. H. Froula, C. Dorrer, E. M. Hill, J. Bromage, T. J. Kessler, J. D. Zuegel, R. K. Follett, L. Nguyen, A. A. Solodov, J. P. Palastro, D. Turnbull, D. H. Edgell, J. G. Shaw, A. M. Hansen, A. L. Milder, J. Katz, R. Boni, V. N. Goncharov, M. Sherlock, H. Le, D. Strozzi, P. Michel, L. Divol, J. F. Myatt, W. Rozmus, J. W. Bates, A. Schmitt, J. Weaver, A. Colaïtis, L. Yin, and B. Albright, "Fourth-Generation Laser for Ultra-Broadband Experiments—Expanding the ICF Design Space Through Mitigation of Laser–Plasma Instabilities."

F. Garcia-Rubio, R. Betti, H. Aluie, and J. Sanz, "The Effect of Self-Generated Magnetic Fields on Ablative Rayleigh–Taylor Instability Dynamics."

V. Yu. Glebov, C. J. Forrest, J. P. Knauer, O. M. Mannion, S. P. Regan, M. H. Romanofsky, T. C. Sangster, and C. Stoeckl, "New Fast Neutron Time-of-Flight Detectors with Subnanosecond Instrument Response Function for DT Implosions on OMEGA."

V. N. Goncharov, S. C. Miller, and P. B. Radha, "A Survey of Different Perturbation Amplification Mechanisms in the Early Stages of Inertial Confinement Fusion Implosions."

V. Gopalaswamy, R. Betti, J. P. Knauer, A. Lees, D. Patel, A. R. Christopherson, K. M. Woo, O. M. Mannion, Z. L. Mohamed, F. J. Marshall, C. Stoeckl, V. Yu. Glebov, S. P. Regan, R. C. Shah, D. H. Edgell, D. Cao, V. N. Goncharov, I. V. Igumenshchev, P. B. Radha, T. J. B. Collins, T. C. Sangster, E. M. Campbell, M. Gatu Johnson, R. D. Petrasso, C. K. Li, and J. A. Frenje, "Improved Predictive Models and Further Progress in the Cryogenic Optimization Campaign on OMEGA."

D. Haberberger, A. Shvydky, V. N. Goncharov, D. Cao, J. Carroll-Nellenback, S. X. Hu, S. T. Ivancic, V. V. Karasiev, J. P. Knauer, A. V. Maximov, and D. H. Froula, "Density Measurements of the Inner Shell Release."

A. M. Hansen, D. Turnbull, R. K. Follett, J. Katz, A. L. Milder, J. P. Palastro, K. L. Nguyen, D. Mastrosimone, D. H. Froula, L. Yin, and B. Albright, "Cross-Beam Energy Transfer Experiments at High-Acoustic Wave Amplitudes."

E. C. Hansen, J. R. Davies, D. H. Barnak, R. Betti, E. M. Campbell, V. Yu. Glebov, J. P. Knauer, J. L. Peebles, A. B. Sefkow, and K. M. Woo, "Neutron Yield Enhancement and Suppression by Magnetization in Laser-Driven Cylindrical Implosions" (invited).

J. Hinz, V. V. Karasiev, S. X. Hu, M. Zaghoo, and D. Mejia-Rodriguez, "First Principles Investigation of the Insulator–Metal Transition in Liquid Hydrogen with a Recently Developed Deorbitalized meta-GGA Exchange-Correlation Functional."

S. X. Hu, R. C. Shah, J. Baltazar, D. Cao, S. P. Regan, V. N. Goncharov, P. B. Radha, J. L. Peebles, W. Theobald, R. Betti, E. M. Campbell, G. Duchateau, A. Casner, and V. T. Tikhonchuk, "Understanding Laser-Imprint Effects on Cryogenic DT Implosions on OMEGA."

I. V. Igumenshchev, R. Betti, E. M. Campbell, D. Cao, C. J. Forrest, V. N. Goncharov, V. Gopalaswamy, J. P. Knauer, O. M. Mannion, D. Patel, S. P. Regan, R. C. Shah, and A. Shvydky, "Three-Dimensional Hydrodynamic Modeling of OMEGA Direct-Drive Cryogenic Implosions with the Highest Fusion Yield."

S. T. Ivancic, F. J. Marshall, W. Theobald, C. Sorce, D. Cao, I. V. Igumenshchev, S. P. Regan, R. C. Shah, J. P. Knauer, V. N. Goncharov, R. Betti, and T. C. Sangster, "Three-Dimensional Gated Hot-Spot X-Ray Imaging on OMEGA."

V. V. Ivanov, A. L. Astanovitskiy, N. L. Wong, K. J. Swanson, I. A. Begishev, J. Bromage, J. R. Davies, A. V. Maximov, C. Mileham, and C. Stoeckl, "Study of Laser-Driven Magnetic Fields in the Coil Target."

V. V. Karasiev, S. X. Hu, and L. Calderin, "Systematic *Ab Initio* Calculations of Optical Properties of Silicon for Inertial Confinement Fusion Applications."

A. Kish, A. B. Sefkow, J. Giuliani, A. Velikovich, S. Zalesak, and A. Schmitt, "Toward Advanced Modeling of Transport in Magnetized Inertial Confinement Fusion Targets."

J. P. Knauer, R. Betti, V. Gopalaswamy, D. Cao, I. V. Igumenshchev, A. Shvydky, D. Patel, A. Lees, M. J. Bonino, E. M. Campbell, T. J. B. Collins, C. J. Forrest, V. Yu. Glebov, V. N. Goncharov, D. R. Harding, J. A. Marozas, F. J. Marshall, P. W. McKenty, P. B. Radha, S. P. Regan, T. C. Sangster, C. Stoeckl, M. Gatu Johnson, J. A. Frenje, and R. D. Petrasso, "The Effect of Laser Bandwidth on High-Performance Cryogenic Implosions."

L. S. Leal, A. V. Maximov, A. B. Sefkow, R. Betti, and V. V. Ivanov, "Three-Dimensional Modeling of Laser–Plasma Confinement in a Strong Magnetic Field."

A. Lees, R. Betti, J. P. Knauer, V. Gopalaswamy, D. Patel, A. R. Christopherson, K. M. Woo, O. M. Mannion, Z. L. Mohamed, F. J. Marshall, C. Stoeckl, V. Yu. Glebov, S. P. Regan, R. C. Shah, D. H. Edgell, C. Cao, V. N. Goncharov, I. V. Igumenshchev, P. B. Radha, T. J. B. Collins, T. C. Sangster, E. M. Campbell, M. Gatu Johnson, R. D. Petrasso, C. K. Li, and J. A. Frenje, "Toward Optimizing Cryogenic Inertial Confinement Fusion Implosions."

O. M. Mannion, C. J. Forrest, D. Cao, V. Yu. Glebov, V. N. Goncharov, V. Gopalaswamy, J. P. Knauer, Z. L. Mohamed, S. P. Regan, T. C. Sangster, C. Stoeckl, A. J. Crilly, B. D. Appelbe, and J. P. Chittenden, "Experimental Analysis of nT Kinematic Edge Data on OMEGA."

J. A. Marozas, P. W. McKenty, T. J. B. Collins, M. J. Rosenberg, P. B. Radha, S. P. Regan, S. Miller, E. M. Campbell, B. E. Blue, L. Divol, W. W. Hsing, G. E. Kemp, C. B. Yeamans, and H. D. Whitley, "NIF Polar-Drive High DT-Yield Exploder-Pusher Designs Modeled Using Pump-Depletion in *DRACO*."

F. J. Marshall, S. T. Ivancic, C. Mileham, P. M. Nilson, J. J. Ruby, B. S. Schiener, M. J. Schmitt, and C. A. Wilde, "High-Resolution X-Ray Imaging with Fresnel Zone Plates on the University of Rochester's OMEGA and OMEGA EP Laser Systems."

A. V. Maximov, D. Turnbull, J. G. Shaw, R. K. Follett, and J. P. Palastro, "Effect of Multibeam Two-Plasmon–Decay Instability on Cross-Beam Energy Transfer in Plasmas."

P. W. McKenty, F. J. Marshall, D. R. Harding, R. S. Craxton, M. J. Rosenberg, J. A. Marozas, T. J. B. Collins, P. B. Radha, E. M. Campbell, B. E. Blue, C. B. Yeamans, W. W. Hsing, and M. Farrell, "Evaluation of Ablator-Shell Contouring to Enhance the Performance of NIF Polar-Drive High-Yield Source Experiments."

A. L. Milder, J. Katz, R. Boni, D. Nelson, J. P. Palastro, K. Daub, R. K. Follett, and D. H. Froula, "Measurements of Arbitrary Electron Distribution Functions Using Angularly Resolved Thomson Scattering."

S. C. Miller, P. B. Radha, V. N. Goncharov, T. J. B. Collins, J. A. Marozas, and A. Shvydky, "A Study of Internal Perturbation Evolution in Inertial Confinement Fusion Implosions."

Z. L. Mohamed, C. J. Forrest, J. P. Knauer, R. Simpson, and M. Gatu Johnson, "Observed Variations in Areal Densities as Measured by Detectors Along Multiple Lines of Sight."

K. L. Nguyen, L. Lin, B. J. Albright, A. M. Hansen, D. H. Froula, D. Turnbull, and J. P. Palastro, "Simulation Study of Nonlinear Saturation of Cross-Beam Energy Transfer in TOP9 Experiments at the Omega Laser Facility."

P. M. Nilson, I. V. Igumenshchev, R. Betti, D. H. Froula, L. Gao, J. Matteucci, W. Fox, M. G. Haines, and D. D. Meyerhofer, "Magnetic Reconnection in the High-Energy-Density Regime" (invited).

J. P. Palastro, J. L. Shaw, D. Ramsey, T. T. Simpson, P. Franke, S. T. Ivancic, K. Daub, and D. H. Froula, "Dephasingless Laser Wakefield Acceleration."

D. Patel, R. Betti, K. M. Woo, V. Gopalaswamy, J. P. Knauer, R. C. Shah, and A. Bose, "Analysis and Reconstruction of Highest-Performing OMEGA DT Layered Implosion Shot 90288."

R. Paul, S. X. Hu, V. V. Karasiev, and S. A. Bonev, "Temperature-Induced Changes in hP4-Sodium Electride: An *Ab Initio* Study."

J. L. Peebles, S. X. Hu, W. Theobald, V. N. Goncharov, N. Whiting, E. M. Campbell, T. R. Boehly, S. P. Regan, P. M. Celliers, S. J. Ali, and G. Duchateau, "Measurements of Laser-Imprint–Induced Shock-Velocity Nonuniformities and Laser-Imprint Mitigation."

D. N. Polsin, G. W. Collins, L. Crandall, X. Gong, R. Saha, M. Huff, G. Tabak, Z. K. Sprowal, T. R. Boehly, M. Zaghoo, J. R. Rygg, P. M. Celliers, D. E. Fratanduono, Y. Ping, J. H. Eggert, D. H. Munro, A. Lazicki, and D. G. Hicks, "X-Ray Diffraction of Double-Shocked Diamond."

P. B. Radha, M. J. Rosenberg, A. Shvydky, W. Theobald, D. Turnbull, F. J. Marshall, K. S. Anderson, R. Betti, E. M. Campbell, V. N. Goncharov, T. J. B. Collins, R. S. Craxton, J. A. Marozas, P. W. McKenty, S. P. Regan, T. C. Sangster, C. B. Yeamans, B. E. Blue, W. W. Hsing, and R. Scott, "Validating Direct-Drive Implosion Energetics Based on OMEGA and NIF Experiments."

D. W. Ramsey, D. H. Froula, and J. P. Palastro, "Vacuum Acceleration in a Flying Focus."

S. P. Regan, O. M. Mannion, C. J. Forrest, J. P. Knauer, R. Betti, E. M. Campbell, D. Cao, V. Yu. Glebov, V. N. Goncharov, S. T. Ivancic, F. J. Marshall, P. B. Radha, T. C. Sangster, R. C. Shah, C. Sorce, C. Stoeckl, and W. Theobald, "Hot-Spot Flow Velocity in Laser-Direct-Drive Inertial Confinement Fusion Implosions."

H. G. Rinderknecht, C. J. Forrest, J. P. Knauer, W. Theobald, S. P. Regan, R. Simpson, M. Gatu Johnson, and J. A. Frenje, "Hot Spot and Fuel Imaging Using Nuclear Diagnostics on Direct-Drive Cryogenic Implosions at OMEGA."

M. J. Rosenberg, A. A. Solodov, W. Seka, R. K. Follett, A. V. Maximov, C. Ren, S. Cao, S. P. Regan, P. B. Radha, T. J. B. Collins, D. H. Froula, J. P. Palastro, V. N. Goncharov, J. F. Myatt, P. A. Michel, M. Hohenberger, G. Swadling, J. S. Ross, R. Scott, and K. Glize, "Hot-Electron Generation Mechanisms in Ignition-Scale Direct-Drive Coronal Plasmas on the NIF."

J. J. Ruby, J. R. Rygg, D. A. Chin, C. J. Forrest, V. Yu. Glebov, C. Stoeckl, G. W. Collins, B. Bachmann, J. A. Gaffney, Y. Ping, N. V. Kabadi, and P. Adrian, "Analysis of Self-Emission from Spherical Shock Experiments."

A. B. Sefkow, J. G. Shaw, J. Carroll-Nellenback, S. Pai, E. G. Blackman, D. Cao, J. R. Davies, R. K. Follett, A. Frank, J. L. Giuliani, M. Haddad, E. C. Hansen, S. B. Hansen, S. X. Hu, A. Kish, M. Lavell, R. L. McCrory, P. W. McKenty, P. M. Nilson, A. Shvydky, R. B. Spielman, A. Tu, A. Velberg, and A. L. Velikovich, "Introduction to TriForce: A Multi-Physics Code for Hybrid Fluid-Kinetic Simulations."

R. C. Shah, I. V. Igumenshchev, C. J. Forrest, K. A. Bauer, E. M. Campbell, D. Cao, V. N. Goncharov, S. Sampat, and S. P. Regan, "Influence of In-Flight Shape on Stagnation Performance in Direct-Drive Laser Implosion Experiments."

J. L. Shaw, M. A. Romo-Gonzales, M. M. McKie, J. P. Palastro, D. H. Froula, P. M. King, N. Lemos, G. J. Williams, H. Chen, and F. Albert, "Microcoulomb-Class Self-Modulated Laser Wakefield Accelerator on OMEGA EP" (invited).

A. Shvydky, D. Haberberger, J. P. Knauer, S. X. Hu, S. T. Ivancic, J. Carroll-Nellenback, D. Cao, I. V. Igumenshchev, V. V. Karasiev, A. V. Maximov, S. P. Regan, P. B. Radha, T. C. Sangster, B. Boni, P. Nilson, V. N. Goncharov, D. H. Froula, and V. A. Smalyuk, "Analysis of Shock-Release OMEGA EP Experiments."

T. T. Simpson, D. H. Froula, and J. P. Palastro, "Nonlinear Self-Focusing of Flying Focus Pulses."

A. A. Solodov, M. J. Rosenberg, A. R. Christopherson, R. Betti, M. Stoeckl, W. Seka, R. Epstein, R. K. Follett, P. B. Radha, S. P. Regan, D. H. Froula, J. P. Palastro, V. N. Goncharov, J. F. Myatt, M. Hohenberger, B. Bachmann, and P. Michel, "Hot-Electron Preheat and Energy Deposition in Direct-Drive Implosion Experiments at the National Ignition Facility."

C. Stoeckl, T. J. B. Collins, R. Epstein, V. N. Goncharov, R. K. Jungquist, C. Mileham, P. B. Radha, S. P. Regan, T. C. Sangster, and W. Theobald, "Investigating Small-Scale Mix in Direct-Drive Cryogenic DT Implosions with Radiography on OMEGA."

W. Theobald, D. Cao, R. C. Shah, K. A. Bauer, R. Betti, M. J. Bonino, E. M. Campbell, A. R. Christopherson, T. J. B. Collins, R. S. Craxton, D. H. Edgell, R. Epstein, C. J. Forrest, R. K. Follett, D. H. Froula, V. Yu. Glebov, V. N. Goncharov, V. Gopalaswamy, D. R. Harding, S. X. Hu, I. V. Igumenshchev, S. T. Ivancic, D. W. Jacobs-Perkins, R. T. Janezic, J. H. Kelly, T. J. Kessler, J. P. Knauer, T. Z. Kosc, O. M. Mannion, J. A. Marozas, F. J. Marshall, P. W. McKenty, Z. L. Mohamed, S. F. B. Morse, P. M. Nilson, J. P. Palastro, D. Patel, J. L. Peebles, P. B. Radha, H. G. Rinderknecht, M. J. Rosenberg, S. Sampat, T. C. Sangster, W. Seka, M. J. Shoup III, W. T. Shmayda, A. Shvydky, C. Sorce, C. Stoeckl, C. Thomas, J. Ulreich, M. D. Wittman, S. P. Regan, B. Rice, M. Gatu Johnson, J. A. Frenje, and R. D. Petrasso, "Enhanced Laser Energy Coupling with Small-Spot Distributed Phase Plates (SG5-650) in OMEGA Cryogenic Implosions."

C. A. Thomas, K. L. Baker, D. T. Casey, M. Hohenberger, A. L. Kritcher, B. K. Spears, S. Khan, R. Nora, T. Woods,

J. L. Milovich, R. L. Berger, D. Strozzi, D. D. Ho, D. Clark, B. Bachmann, R. Benedetti, R. Bionta, P. M. Celliers, D. Fittinghoff, G. Grim, R. Hatarik, N. Izumi, G. Kyrala, T. Ma, M. Millot, S. R. Nagel, P. K. Patel, C. B. Yeamans, M. Tabak, M. Gatu Johnson, P. L. Volegov, and E. M. Campbell, "Review of BigFoot Implosion Data at NIF."

D. Turnbull, D. Cao, D. H. Edgell, R. K. Follett, D. H. Froula, V. N. Goncharov, A. V. Maximov, J. P. Palastro, W. Seka, C. Stoeckl, and H. Wen, "Anomalous Absorption by the Two-Plasmon–Decay Instability in Directly Driven Inertial Confinement Fusion Experiments."

D. Turnbull, C. Dorrer, D. H. Edgell, R. K. Follett, D. H. Froula, A. M. Hansen, J. Katz, B. E. Kruschwitz, A. L. Milder, J. P. Palastro, A. Colaitis, T. Chapman, L. Divol, C. S. Goyon, P. Michel, J. D. Moody, B. B. Pollock, J. S. Ross, and D. J. Strozzi, "Impact of Non-Maxwellian Electron Distribution Functions on Crossed-Beam Energy Transfer" (invited).

H. Wen, B. J. Winjum, F. S. Tsung, and W. B. Mori, "Mitigation of Stimulated Raman Scattering with Laser Bandwidth and an External Magnetic Field."

J. Wilson, V. N. Goncharov, T. Simpson, D. Ramsey, C. Dorrer, A. Shvydky, D. H. Froula, and J. P. Palastro, "Broadband Smoothing of Laser Pulses for Imprint Reduction in Direct-Drive Inertial Confinement Fusion."

K. M. Woo, R. Betti, O. M. Mannion, D. Patel, C. J. Forrest, J. P. Knauer, V. N. Goncharov, P. B. Radha, K. S. Anderson, R. Epstein, J. A. Delettrez, M. Charissis, A. Shvydky, I. V. Igumenshchev, V. Gopalaswamy, A. R. Christopherson, Z. L. Mohamed, D. Cao, H. Aluie, E. M. Campbell, R. Yan, P.-Y. Chang, A. Bose, D. Shvarts, and J. Sanz, "Inferring the Thermal Ion Temperature and Residual Kinetic Energy from Nuclear Measurements in Inertial Confinement Fusion" (invited).

S. Zhang, H. Whitley, L. Benedict, L. Yang, K. Caspersen, J. Gaffney, M. Däne, J. Pask, P. Sterne, T. Ogitsu, A. Lazicki, M. Marshall, D. Swift, M. Martin, R. London, A. Kritcher, J. Nilsen, N. Kostinski, B. Maddox, B. Militzer, K. Driver, F. Soubiran, A. Sharma, P. Suryanarayana, D. D. Johnson, A. V. Smirnov, S. X. Hu, and W. Johnson, "Wide-Range EOS of Carbon and Boron Materials from First Principles."

M. S. Wei, "Status FY19 OLUG Findings and Recommendations," presented at the APS DPP OLUG Update, Fort Lauderdale, FL, 22 October 2019.

S. G. Demos, "Optical Materials Research at LLE," presented at the CEA Seminar, Bordeaux, France, 23 October 2019.

S. G. Demos, "Relocation of the SPIE Laser Damage Conference to Rochester and Opportunities for Industrial Partners," presented at the Institute of Optics 2019 Fall Industrial Associates Symposium, Rochester, NY, 1 November 2019.

The following presentations were made at the 2nd American Physical Society Division of Plasma Physics Community Planning Process Workshop for High Energy Density Physics (HEDP), Palo Alto, CA, 11–14 November 2019:

J. P. Palastro, D. H. Froula, J. L. Shaw, T. M. Antonsen, J. Vieira, N. Vafaei-Najafabadi, W. Mori, P. Franke, D. Ramsey, T. T. Simpson, K. Daub, M. S. Wei, J. D. Zuegel, and E. M. Campbell, "Spatiotemporally Structured Light for Advanced Accelerators and Radiation Sources."

J. D. Zuegel, J. Bromage, D. H. Froula, M. S. Wei, H. G. Rinderknecht, P. M. Nilson, S. X. Hu, F. Albert, B. M. Hegelich, M. Roth, and E. M. Campbell, "Frontiers in High-Energy-Density and Relativistic Plasma Physics Enabled by EP OPAL: A Multibeam Ultrahigh-Intensity Laser User Facility."

K. L. Marshall, T. Z. Kosc, B. N. Hoffman, S. Papernov, A. A. Kozlov, S. G. Demos, J. Shojaie, C. Dorrer, D. Batesky, J. Wallace, S. Jacobs, A. Schmid, K. Richardson, J. Starowitz, S. H. Chen, T. Brown, and N. Tabiryan, "Liquid Crystal Research at LLE: A 35-Year Journey from Information Displays to Laser Fusion and Beyond," presented at the Rochester OSA/SPIE Student Chapter Lecture Series, Rochester, NY, 12 November 2019.

M. S. Wei, "Overview of Fundamental Science Programs at the Omega Laser Facility," presented at the SUNY Geneseo Colloquium, Geneseo, NY, 21 November 2019.

The following presentations were made at the Materials Research Society Fall Meeting, Boston, MA, 1–6 December 2019:

J. M. Garcia Figueroa and D. R. Harding, "The Relationship Between the Processing Conditions for an Electron Cyclotron Resonance-(ECR) Microwave-(MW) CVD System and the Properties of Vapor Deposited Hydrocarbon Films."

M. Wang and D. R. Harding, "Mechanical Properties of Micrometer-Size Cellular Foam-Like Auxetic Structures."

The following presentations were made at the Conference on High Intensity Laser and Attosecond Science in Israel, Tel Aviv, Israel, 9–11 December 2019:

R. Betti, V. Gopalaswamy, J. P. Knauer, A. R. Christopherson, D. Patel, K. M. Woo, A. Bose, K. S. Anderson, T. J. B. Collins, S. X. Hu, D. T. Michel, C. J. Forrest, R. C. Shah, P. B. Radha, V. N. Goncharov, V. Yu. Glebov, A. V. Maximov, C. Stoeckl, F. J. Marshall, M. J. Bonino, D. R. Harding, R. T. Janezic, J. H. Kelly, S. Sampat, T. C. Sangster, S. P. Regan, E. M. Campbell, M. Gatu Johnson, J. A. Frenje, C. K. Li, and R. D. Petrasso, "Overview of the Cryogenic Implosion Campaign on the OMEGA Laser."

S. P. Regan, V. N. Goncharov, T. C. Sangster, R. Betti, E. M. Campbell, K. A. Bauer, M. J. Bonino, D. Cao, G. W. Collins, T. J. B. Collins, R. S. Craxton, D. H. Edgell, R. Epstein, C. J. Forrest, J. A. Frenje, D. H. Froula, M. Gatu Johnson, V. Yu. Glebov, V. Gopalaswamy, D. R. Harding, S. X. Hu, I. V. Igumenshchev, S. T. Ivancic, D. W. Jacobs-Perkins, R. T. Janezic, T. J. Kessler, J. P. Knauer, T. Z. Kosc, J. Kwiatkowski, O. M. Mannion, J. A. Marozas, F. J. Marshall, P. W. McKenty, Z. L. Mohamed, S. F. B. Morse, P. M. Nilson, J. P. Palastro, D. Patel, J. L. Peebles, R. D. Petrasso, P. B. Radha, H. G. Rinderknecht, M. J. Rosenberg, S. Sampat, W. Seka, R. C. Shah, J. R. Rygg, W. T. Shmayda, M. J. Shoup III, A. Shvydky, A. A. Solodov, C. Sorce, C. Stoeckl, W. Theobald, D. Turnbull, J. Ulreich, M. D. Wittman, and K. M. Woo, "Three-Dimensional Diagnostics for Inertial Confinement Fusion Research on OMEGA" (invited).